UNIVERSIDAD DE INVESTIGACIÓN DE TECNOLOGÍA EXPERIMENTAL YACHAY

Escuela de Ciencias Físicas y Nanotecnología

Understanding the formation and evolution of galactic superbubbles

Trabajo de integración curricular presentado como requisito para la obtención del título de Físico/a.

Autor:

Suárez López Osmer Alexander

Tutor:

Banda Barragán Wladimir, Ph.D.

Urcuquí, abril 2024

AUTORÍA

Yo, **Osmer Alexander Suárez López**, con cédula de identidad 1004668123, declaro que las ideas, juicios, valoraciones, interpretaciones, consultas bibliográficas, definiciones y conceptualizaciones expuestas en el presente trabajo; así cómo, los procedimientos y herramientas utilizadas en la investigación, son de absoluta responsabilidad de el/la autora (a) del trabajo de integración curricular. Así mismo, me acojo a los reglamentos internos de la Universidad de Investigación de Tecnología Experimental Yachay.

Urcuquí, Abril 2024.

Osmer Alexander Suárez López
CI: 1004668123

AUTORIZACIÓN DE PUBLICACIÓN

Yo, **Osmer Alexander Suárez López**, con cédula de identidad 1004668123, cedo a la Universidad de Investigación de Tecnología Experimental Yachay, los derechos de publicación de la presente obra, sin que deba haber un reconocimiento económico por este concepto. Declaro además que el texto del presente trabajo de titulación no podrá ser cedido a ninguna empresa editorial para su publicación u otros fines, sin contar previamente con la autorización escrita de la Universidad.

Asimismo, autorizo a la Universidad que realice la digitalización y publicación de este trabajo de integración curricular en el repositorio virtual, de conformidad a lo dispuesto en el Art. 144 de la Ley Orgánica de Educación Superior

Urcuquí, Abril 2024.

Osmer Alexander Suárez López
CI: 1004668123

Dedication

To my mother and brother

Acknowledgements

To my family, especially to my mother, who has always been my unconditional support and, in spite of the adversities, knew how to get me through the day. Furthermore, to my grandparents who did and do everything for me. I would also like to express my gratitude to my tutor and friend, Wladimir Banda, for his inspiring teachings and motivating influence that have contributed to my personal and academic development.

Osmer Suárez-López

Resumen

Las superburbujas galácticas son estructuras en forma de lóbulo que son creadas por episodios intensos de formación estelar, que ocurren en los discos de galaxias espirales. Los procesos de formación estelar son mecanismos de retroalimentación importantes en tales galaxias, ya que permiten el intercambio de gas y polvo entre los medios interestelar y circungaláctico. Observacionalmente, las superburbujas se detectan mediante estudios de líneas de emisión o absorción de especies atómicas y moleculares, pero la información del telescopio está proyectada, por lo que se necesitan simulaciones numéricas para entender su estructura tridimensional. En esta tesis recurrimos a simulaciones hidrodinámicas para estudiar numéricamente la estructura tridimensional de tales superburbujas. Incluimos atmósferas galácticas estratificadas utilizando prescripciones analíticas, que luego se utilizan como condiciones iniciales en nuestros modelos numéricos. Nuestras simulaciones exploran el efecto de cambiar el parámetro de fuerza de turbulencia (σ_t), que controla la morfología del disco, su distribución inicial de nubes y el perfil cinemático de la atmósfera. Encontramos que las superburbujas galácticas surgen de las interacciones entre los vientos de formación estelar y el medio interestelar en el disco. Su formación es favorecida por valores más altos de σ_t, ya que permiten un mecanismo de canalización mejor que los valores bajos de σ_t. Al final, se necesitan $\sigma_t > 60, \mathrm{km, s^{-1}}$ para producir superburbujas que se asemejen a las encontradas en el centro galáctico de la Vía Láctea. Estudios recientes muestran que el centro galáctico alberga una chimenea en dirección norte, que actualmente carece de una explicación teórica. Este estudio contribuye a la comprensión de esta característica.

Palabras clave: Superburbujas, Formación estelar, Simulaciones hidrodinámicas, Atmósfera galáctica, Chimenea, Mecanismo de retroalimentación.

Abstract

Galactic superbubbles are lobe-like structures that are created by intense episodes of star formation, occurring in the discs of spiral galaxies. Star formation processes are important feedback mechanisms in such galaxies as they permit the exchange of gas and dust between the interstellar and circumgalactic media. Observationally, superbubbles are detected via emission or absorption line studies of atomic and molecular species, but telescope information is projected, so numerical simulations are needed to understand their 3D structure. In this thesis we resort to hydrodynamical simulations to numerically study the 3D structure of such superbubbles. We include stratified galactic atmospheres using analytical prescriptions, which are then used as initial conditions in our numerical models. Our simulations explore the effect of changing the turbulence strength parameter (σ_t), which controls the disc morphology, its initial cloud distribution, and the atmosphere kinematical profile. We find that galactic superbubbles arise from interactions between SF winds and the ISM in the disc. Their formation is favoured by higher σ_t values, as they allow for a better channeling mechanism than low σ_t. At the end, $\sigma_\mathrm{t} > 60\,\mathrm{km\,s^{-1}}$ are needed to produce superbubbles that resemble those found in the Galactic centre of the Milky Way. Recent studies show that the Galactic centre harbours a chimney in the northern direction, which currently lacks a theoretical explanation. This study contributes to the understanding of this feature.

Keywords: Superbubbles, Star formation, Hydrodynamical simulations, Galactic atmosphere, Chimney, Feedback mechanism.

Contents

List of Figures

List of Tables

List of Papers

[1] Suárez-López, O.; Villares, A. S.; Banda-Barragán, W. E. Galactic Superbubbles in 3D: Wind Formation and Cloud Shielding. *submitted to Journal of Physics: Conference Series* **2024**.

Chapter 1

Introduction

The Milky Way, as a dynamic spiral galaxy, has been constantly evolving during the last $\sim$ 13 billion years (see Maosheng & Hans-Walter[3]) until reaching the morphology that can be observed today. Our Galaxy is not an isolated system, but it interacts with other galaxies in the so-called Local group (see Maosheng & Hans-Walter[3]). Within Our Galaxy, one of the most important process is star formation (SF) because this process is not only related with the creation of stars, but it also permits the expulsion of gas from the interstellar medium (ISM), i.e. from the disc of the galaxies, into the circumgalactic medium (CGM), i.e. the gas enveloping the galaxies. SF is therefore a type of feedback mechanism, so studies of galactic outflows and the feedback of CGM are important for understanding the formation and evolution of galaxies (see Ponti et al. 2021[4]; Tumlinson et al. 2017[5]; Mayya et al. 2023[6]).

In the ISM a complete equilibrium is not present and SF is a result of such dynamical nature. Stars are in a state of continuous evolution as time unfolds. During their lifetimes, these celestial bodies undergo a process of mass loss, which forms the so-called stellar winds. Stellar winds manifest as a consequence of matter fluxes being expelled during thermal pulses, a phenomenon arising from helium ignition within the star's shell, which is relevant for the more massive stars towards the end of their life, thus it is an specific type of intense stellar winds. In order to detect them it is necessary to use UV spectra obtained with e.g. the IUE satellite (see Carraro 2021[7]). This intricate progression becomes apparent as stars evolve transitioning to the giant branch phase (see e.g. Maoz 2016[8]). In addition, at the end of their lifetime, some stars (the more massive ones with $M > 8$ $M_{\odot}$) also have the capacity to explode as supernovae (SNe). SNe are the final stage of a star, these explosions release enormous amounts of energy and matter into the environment, e.g. type II supernovae that are related to the end of the star due to the collapse of its core. At the galactic scale the combined feedback from stellar winds and SN explosions lead to the formation of the so-called "galactic winds". They are produced by the presence of supernova (SN) events*, and play a substantial role in shaping and influencing the Galactic environment.

The study of galactic winds is still growing, and it is crucial to understand more about this winds because they play an important role in regulating how mater and energy are transported out of the dense regions of star-forming

---

*Galactic winds are also produced by Active Galactic Nuclei, i.e. by black hole activity at the centres of galaxies, but we do not study such winds here. We limit our study to galactic winds produced by stellar feedback.
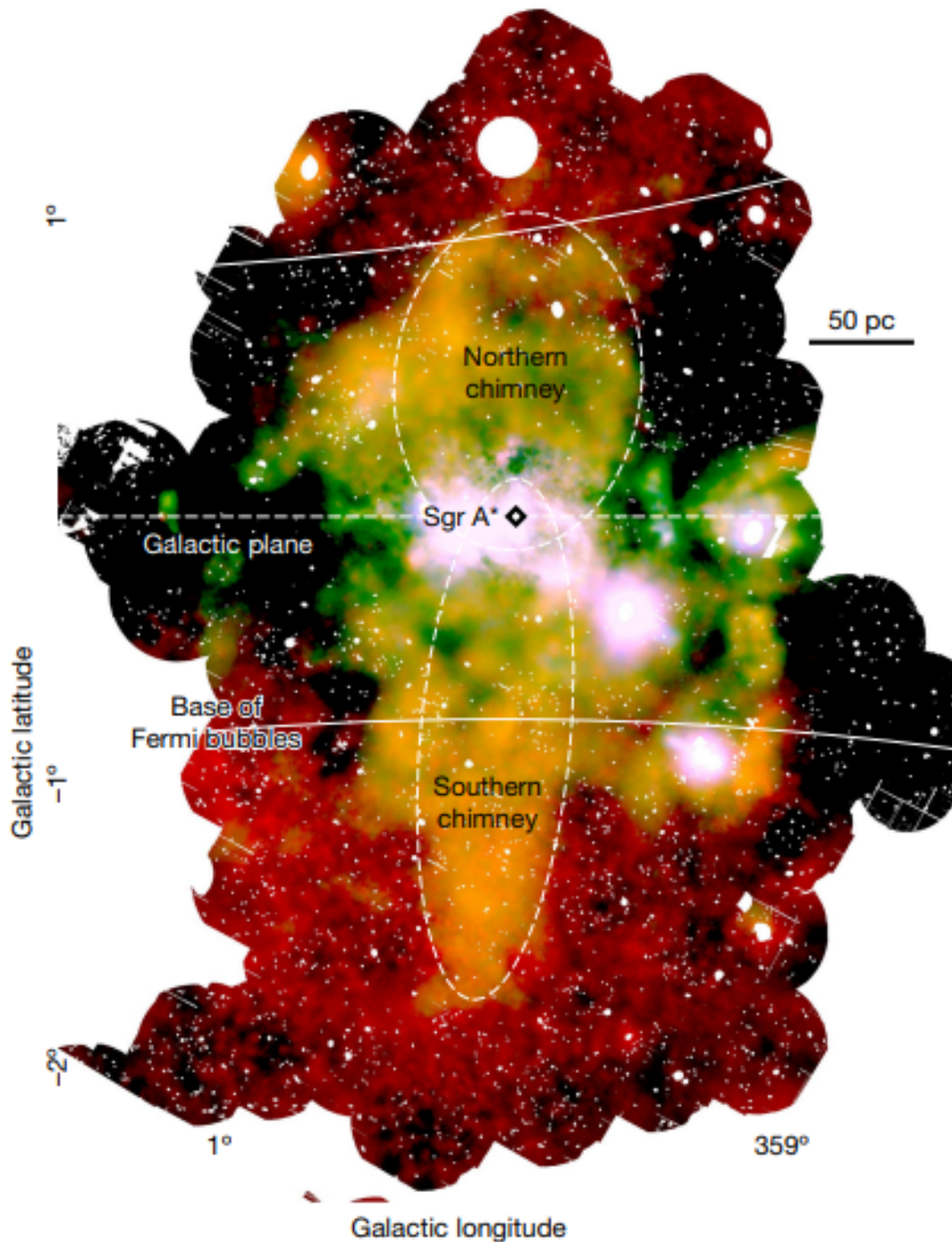
Figure 1.1: Central region of the Milky Way (300 pc by 500 pc) in X-ray emission taken from Ponti et al. 2019[9]. The RGB image combines emissions: red for the 1.5–2.6 keV range, green for S xv transition (2.35–2.56 keV) i.e. X-rays from sulfur ions undergoing a transition, and uncontaminated continuum emission blue (2.7–2.97 keV), i.e. absence of interference of S xv and Ar xvii lines. It includes dashed-line contours for the northern chimney (more spherical shape) and for the southern chimney (more elongated form). It also provides the location of our Galaxy's central black hole Sgr A*.

galaxies, and in particular of our own Galaxy (see Veena et al. 2023[10]; Cicone et al. 2016[11]; Dawson 2013[12]). Indeed, with the purpose of understanding more about those outflows, the Galactic Center (GC) is definitely where we need to look, specifically on spatial scales spanning hundreds of parsecs around the center, because there the rate of SF is larger than in other regions of the Galaxy and there is evidence of a large-scale stellar-driven galactic wind (see e.g. Ponti et al. 2021[4]; Ponti et al. 2019[9]; Snowden et al 1998[13]; Crocker 2012[14]). Now, how to detect these outflows? The answer is multi-wavelength observations. For instance, X-ray observations of the central region of our Galaxy provide information about hot gas dynamics and their interaction with the surrounding environment, and also the high frequency resolution radio continuum observations provided relevant information about the effects of star formation on the Galactic centre's ISM. Observations in these two wavelengths have been used to map the presence of a galactic wind in the GC (see e.g. Nakashima et al. 2019[15]; Predehl et al. 2020[16]; Heywood et al. 2019[17]; Zhang, Li & Morris. 2021[18]).

The GC is then a region of intense SF with a large number of supernova explosions (SNe). Such those explosions have ejected a lot of material with masses of order 1-10 $M_\odot$ per SNe, and energies of order 3×10^{51}erg per SNe (see Maoz. 2016[8]), which upon interactions with the surrounding ISM can inflate hot superbubbles with cold-gas shells as boundaries. It is important to know that such neutral hydrogen (H_I) shells are formed by stellar winds, however in the case of large structures as supperbubbles, they need an energy greater than 10^{53}erg, so in relation with the energy of a SN, it is possible to say that hundreds of SNe are necessary to inflate them (see McClure-Griffiths et al. 2006[19]). All the material flowing out of SNe is known as supernova remnant (SNR), and such amount of matter can fill huge cavities in the space that surrounds SF regions. Sometimes those remnants can disrupt less dense cavities and leave them (see e.g. Ponti et al. 2019[9]; Zhou et al. 2023[20]). Therefore, our interest is on the shell structures (i.e. the filled cavities by SNR), that are also known as chimneys (disrupted ones) and superbubbles (undisrupted ones). Superbubbles take shape across millions of years, following the demise of thousands of stars and the interaction with the ISM (see Sánchez-Cruces & Rosado. 2023[21]). Therefore, they are fundamental for the exchange of materials and energy between the ISM and the CGM in our Galaxy.

In the Milky Way there exists lobe-like structures that emerge from the center of our Galaxy in opposite directions, one to the north and the other one to the south of the Galactic plane. Those supperbubbles were detected by X-ray observations (see Figure1.1) and also by radio continuum observations (see Figure 1.2). Besides, both superbubbles have the same comparable brightness and color in the RGB image (Figure 1.1), which tell us that they share the same origin and emission mechanism. Nevertheless, the morphology of the two supershells diverges. Their configurations lack symmetry with respect to the Galactic plane (see Ponti et al. 2021[4]). In Figure 1.2 it is possible to analyze in much more detail the boundaries and shape of the superbubbles. The southern shell has a more elongated form, even though the components of both the boundaries and the interior of the superbubbles are similar in both structures. This brings some questions, e.g., what is the main feedback mechanism responsible for inflating these superbubbles, SF or AGN? What could be the primary factor driving the disparity in shapes? There are several hypotheses attempting to address these questions, yet none of them provides a definite answer.

To provide answers to these questions, additional astronomical observations have been performed, e.g. Veena et al. 2023[10] have found molecular shells potentially coincident with the walls of these supershells. Also, at much larger scales (of 8 kpc see Fig. 1.3) the so-called Fermi bubbles have been reported in various wavelengths (Carretti
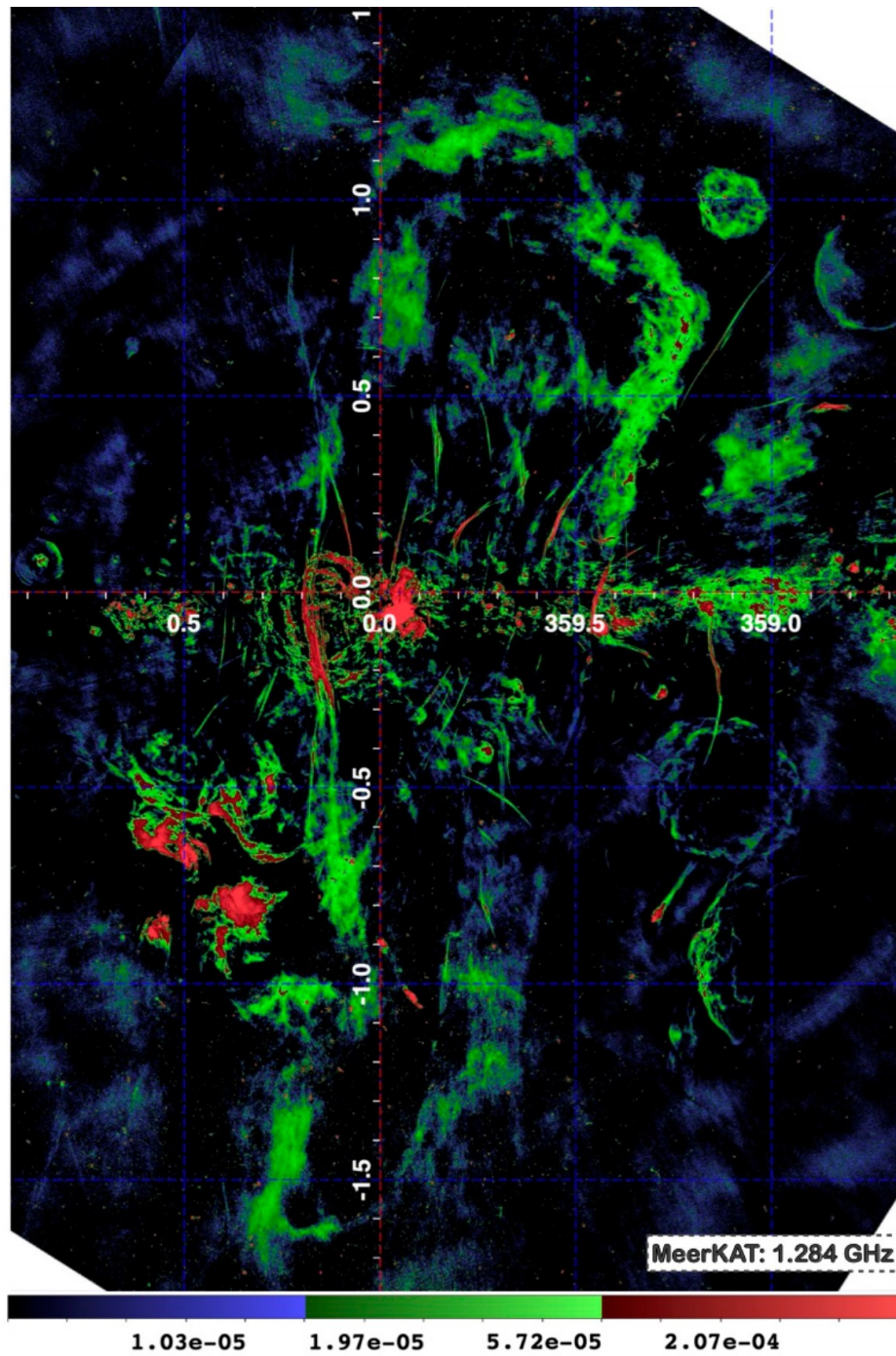
Figure 1.2:   MeerKAT image displayed with its entire dynamical range, and retrieved from Ponti et al. 2021[4]. It can be noticed the boundaries of the GC supperbubbles (green).
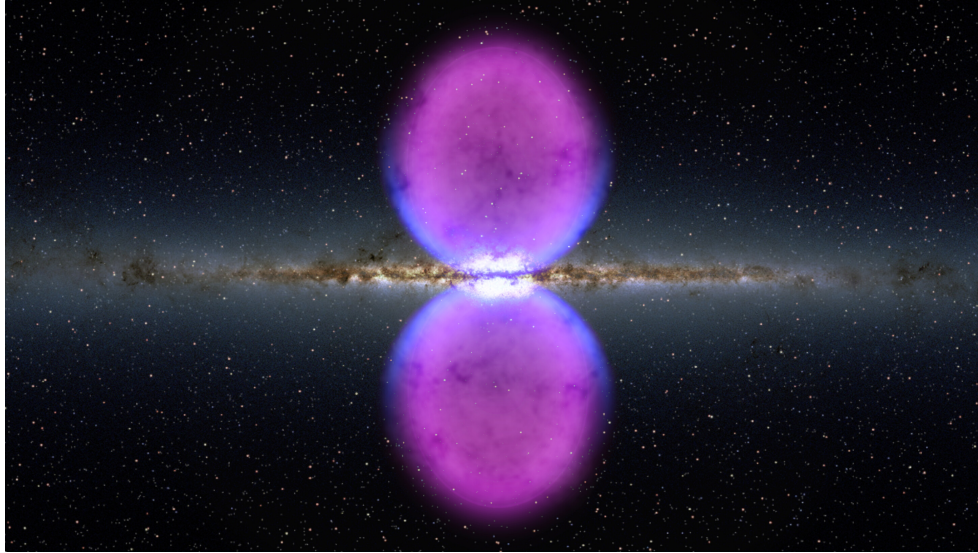
Figure 1.3: Fermi-bubbles size reaches about 15 kpc, it is possible to see Gamma emission (magenta) and X-ray emission at the edges (blue), image retrieved from Mann 2023[1].

et al 2013[22], Su et al. 2010[23]). There is also a galactic wind in starburst galaxy M82 clearly visible in H_α light (see Cooper et al. 2008[24]), which as a consequence gives rise to the formation of superbubbles, because they provide a good environment for the origin of these winds. Aspiring to understand how the nuclear wind in our Galaxy formed in more depth, computational simulations are essential as they can help with addressing complex issues that may not be easily solvable through observational results. At the same time, they can be helpful to infer the properties of galactic winds in other galaxies and even at high redshifts, which are more difficult to interpret.

In this context, the entire timeline and series of feedback processes, including phenomena like SNe, that lead to the development of such structures can be effectively modeled using different ISM/CGM-wind models that integrate hydrodynamic principles. There are small-scale wind-cloud models, e.g. Schneider & Robertson 2017[25]), medium-scale wind-multicloud models (Banda-Barragan et al. 2021[26]), and large-scale disc-wind models (Schneider et al. 2020[27]). In particular, disc-wind models involve establishing specific initial and boundary conditions, including the shape and size of the initial SN-feedback region as well as constructing stratified galactic atmospheres based on analytical prescriptions. The simulations also require a SN energy feedback injection recipe in order to convert it into kinetic winds. This input could come in two forms: thermal and kinetic (see Oppenheimer & Davé 2008[28]). Additionally, it is crucial to acknowledge that the medium in which the superbubbles are situated is not homogeneous. Therefore, applying conditions for an inhomogeneous disc becomes imperative as they influence the formation of the winds (see Cooper et al. 2008[24]).

Throughout simulations, it is possible to analyze how those structures were formed, and the reason behind the outflows produced. In order to accomplish this, it is feasible to compare various models that closely resemble real

astrophysical settings for the CGM.

1.1   Problem Statement

In the center of our Galaxy millions of stars have come to an end producing energetic explosions, supernovae, which have given rise to large-scale winds. Such winds carry all the ejected material away from the supernova remnants in the disc and inflate hot gas bubbles that can encompass large cavities, thus forming large lobe-like structures known as superbubbles. These objects play a crucial role in the interchange of matter between the ISM and the CGM and are important for studying Galactic evolution. Observations at X-ray and radio wavelengths have found two superbubbles located north and south of the Galactic plane. However, these two structures are not completely symmetric in relation to the origin (see Ponti et al. 2019[9]; Ponti et al. 2021[4]). What is the origin of those outflows and how can a turbulent atmosphere influence the distribution and shape of the outflow? Addressing these question holds significance given that it can facilitate a comprehension of these structures and their interconnection with the process of SF.

1.2   General and Specific Objectives

The aim of this study is to understand what is the principal factor contributing to the lack of symmetry of the southern supperbubble in the GC of the Milky Way is, with relation to the northern one, by conducting a series of three-dimensional hydrodynamic simulations of disc-wind systems. The simulations will provide us with valuable information about the evolution of the gas during millions of years, based on initial conditions with stratified galactic atmospheres. Furthermore, our simulations survey over the disc morphology, its initial cloud distribution, and the atmosphere kinematic profile, in order to determine the cause of the shape of the southern chimney. To reach this objective, it is necessary to achieve the following specific objectives:

- Characterize the initial conditions of canonical star-forming galaxies, like gravitational potential and atmosphere, via analytical prescriptions and implement them in the hydrodynamical disc-wind simulations.

- Construct a fractal distribution for the ISM gas, in order to seed turbulence in the atmosphere and observe how this influences the development of the galactic winds.

- Implement a C-based mass and energy injection recipe in our hydrodynamical setup, with the aim of replicating the SF activity in the GC.

- Study the evolution and physical properties of the disc-wind gas via 2D projections, phase diagrams and 3D plots of various grid-based quantities defined inside our computational domains.

- Compare 3 models with different values for the turbulence strength parameter (σ_t) and compare their evolution.

The structure of this thesis is the following: Chapter 2 is an overview of the theoretical background of galactic wind models and the components of the Galaxy are presented, along with an study of the gravitational and density

field of the ISM. Chapter 3 provides an overview of the approach and initial parameters utilized in the project. This encompasses detailing the software and computational instruments employed for conducting simulations and analyzing data. Chapter 4 presents the results followed by an in-depth discussion of the models with observations, also the caveats and limitations of the project. Finally, Chapter 5 shows the discoveries of this thesis, and summarize the final conclusions.

Chapter 2

Theory of Galaxy Evolution

Galaxies serve the exclusive domains where stars take residence. These vast astronomical entities comprise millions of stars (ranging from 10^7 to 10^{11}), arranged in diverse configurations, with spiral and elliptical galaxies being the most prevalent. Throughout the Universe, galaxies undergo transformative evolutionary paths, initiated by gravitational interactions since their formation, thus giving rise to the birth of stars and winds. Nonetheless, stars are not the sole constituent of galaxies. In the subsequent sections, we delineate essential characteristics defining a spiral galaxy, aiming to establish a framework for understanding the structure and essential scales of star-forming galaxies (such as the MW and M82), crucial for simulation studies.

2.1   The Milky Way structure

The exploration of the Milky Way commenced with early observations of mostly the Solar neighbourhood, only since the 1920s it has witnessed a substantial leap in our comprehension of our Galactic home. This advancement is primarily attributed to technological breakthroughs in observational methodologies (see Gribbin 2008[29]). Presently, the astronomical landscape is enriched by the presence of large optical telescopes, complemented by the capabilities of radio and X-ray telescopes. These sophisticated instruments have provided data, enabling the scrutiny of fainter regions and celestial entities within our Galaxy. This wealth of information not only serves as a foundation for comparative analyses with theoretical models and computational simulations, but it also facilitates a profound exploration of the structure inherent to our Galaxy, thereby affording us an enhanced understanding of spiral galaxies in general.

To comprehend the intricacies of the Milky Way's structure, it is crucial to delve into the processes that led to the formation of our Galaxy. Based on observational data and numerical modelling, a prevalent formation model relies on the rapid collapse of a primordial spherical gas cloud, with some gradients of density as the origin of the Galactic disc. During the collapse, SF also started, and these old stars it produced are crucial to understand some properties of the initial Galaxy because they still have imprints on the orbits and the chemical composition of the primordial gas as well as its history until now (see Robertson 2022[30]; Hernández-Aguayo et al. 2021[31]). However, the collapse
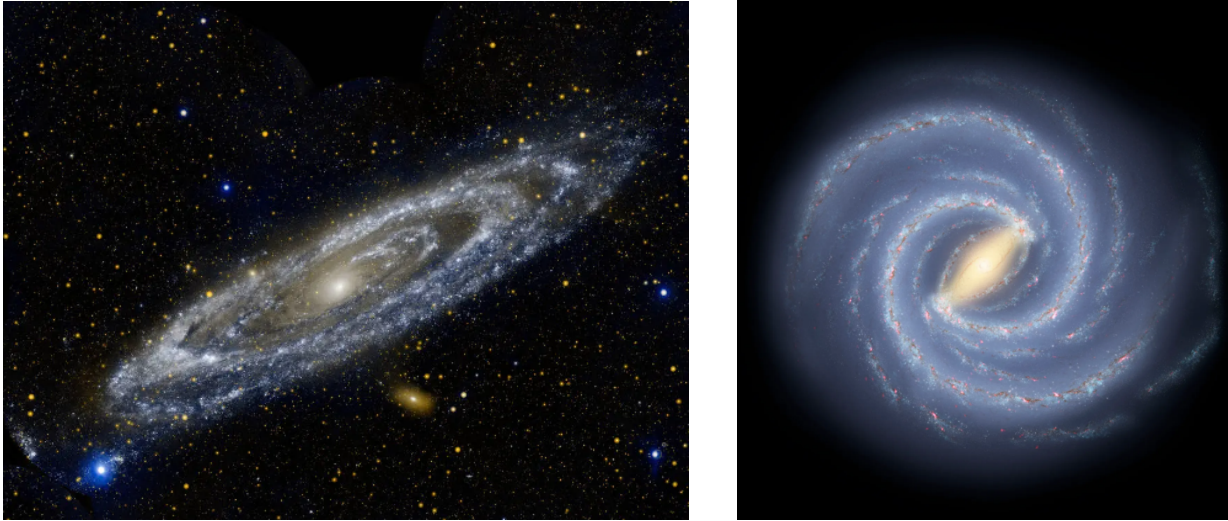
Figure 2.1: Different perspectives of spiral galaxies. Left: Andromeda. Right: Sketch of the Milky Way Galaxy. Retrieved from: NASA Images Galleries, https://www.nasa.gov/image-galleries/.

faced constraints along the X and Y axes owing to the emerging rotational velocity driven by angular momentum conservation. Notably, in the Z axis prevailed the collapse, therefore, the Galaxy flattened into a disc shape, where dissipation of energy due to collisions is also ubiquitous (refer to Majewski 1993[32]).

In Figure 2.1, we can see the Andromeda (left panel) and Milky Way (right panel) galaxies, both belonging to the spiral galaxy type. With the naked eye it is possible to determine the structures that galaxies of this type contain, for example the disc, the spheroid or bulge near the centre, the spiral structure of the ISM and the regions of SF, plus star clusters and ISM dust. Nevertheless, there are other components, that we cannot see in Figure 2.1. Such structures are the halo, the supermassive black hole, cosmic rays, and the dark matter halo. According to Shuter 2012[33], there are 4 important components in our Galaxy, which are the bulge or spheroid with 5 kpc or radius, the central disc, where the spiral arms are located with 15 kpc of radius, the halo and the outer halo or corona with radii of 20 and 60 kpc respectively. Below, the relevant components for the research are addressed in more depth.

2.1.1   The ISM Disc

The greater concentration of stars in our Galaxy is in the disc, which could be subdivided in two components. The first component is the stellar disc, contains most of the stars of the Galaxy, and is where the SF process takes place. This region is shaped into spiral arms, which shows more luminosity because of the higher star density concentration and also by the presence of O and B stars and H_{II} regions. Besides, in this region the Population I type stars are found, and the spiral form is explained by introducing density waves (see Gribbin 2008[29]; Maoz 2016[8]). The second

component is the gas-and-dust disc, characterized by a larger scale height compared to the stellar disc and it is responsible for the extinction in the Galaxy, with a factor of $\sim 10^{11}$ at visible wavelengths.

The density of the disc is variable and depends on the radial coordinate with respect to the GC r and on the disc height z, which decreases in an exponential way and it is described as follows:

$$\rho(r,z) = \rho_0 e^{-\frac{r}{r_d}} e^{-\frac{|z|}{h_d}} \tag{2.1}$$

Where r_d is the scaled length of the disc and has a value of 2.5 ± 0.5 kpc, and h_d is the scaled height with values of 400 pc for the older stars in the disc and 130 pc for the gas-and-dust disc. Also it is important to mention that the mass of the disc $M_{disc} \sim 10^{10} M_\odot$ (see e.g. Maoz 2016[8]; Shuter 2012[33]).

2.1.2 The Stellar Spheroid

The spheroid, as the disc, consists of two components; a central bulge of approximately 1 kpc of radius, and spherical halo of ~ 50 kpc of radius approximately. Furthermore, the density in the central bulge has correlation with the radius. It is inversely proportional to the cube of the distance to the center ($\rho \sim r^{-3}$). In addition, the halo contains around 200 globular clusters. In the spheroid the Population II stars resides (i.e. old stars). The three dimensional shape of the spheroid is a body of revolution of elliptical shape about its minor axis, which results in an oblate spheroid. The mass of the spheroid is e.g. $M_{ss} \sim 10^9 M_\odot$.

For a more comprehensive understanding of the central bulge, Shuter (2012)[33] has highlighted that this sector of the Milky Way is comprised of distinct regions or rings, starting with the giant molecular clouds ring. Then at 3 kpc from the center it is the Oort-Rougoor spiral, which contains H_I and is rotating and expanding. Continuing to the center, we find the Burton-Liszt tilted feature at 1.5 kpc from the center. This region contains H_I and molecular hydrogen. At 0.3 kpc it is another ring, which contains a mixture of H_I, H_{II}, and H_2, so it is here where the most intense SF process occurs. At smaller radii, we find the central molecular zone (see e.g. Morris and Serabyn 1996[34]) and within it several clouds, such as Sgr B2 (Armijos-Abendaño et al. 2020[35]), Sgr C (Nogueras-Lara 2024[36]), a warmish cloud is found at 10 pc, where it is possible to find a combination of gas and molecules, and inside the 3 pc there are the Rodriguez and Chaisson compact clouds (see Shuter (2012)[33]).

2.1.3 Galactic Winds

Galactic chimneys are formed after several Myr of intense SF episodes. As we mentioned in the previous chapter, the formation of these structures is related with intense explosions, (i.e. thousands of SNe), which result in the formation of a collection of SNR in cavities and lobe structures that propagate outwards, thus facilitating the exchange of material between the ISM and the CGM. However, something that was not addressed in a very exhaustive manner and is important to know as a consequence of this feedback mechanism, is the powerful galactic winds that can be driven from smaller-scale chimneys and bubbles. The estimated total energy of stellar-driven galactic winds is $10^{54} \leq E \leq 10^{58}$erg; their velocities can be $v \gtrsim 10^3$km s^{-1}) (see Strickland & Stevens 2000[37]).

According to Strickland & Stevens 2000[37], galactic winds can be detected in several ways along the minor axis of the galaxy and in a collimated flow: filamentary optical emission-line gas, soft thermal X-ray emission,

and non-thermal radio emission, are some of the signatures of a galactic wind. Furthermore, these winds hold importance in several ways, for example: they serve a feedback mechanism for CGM, as a reheating source of the intergalactic medium, and also as an extreme form of SF feedback for the ISM, regulating the SF rates and structuring the ISM. These make them important for galaxy formation and evolution (see Strickland & Stevens 2000[37]). Given the importance of winds, it is crucial to understand better their properties and build models to make more quantitative predictions for observations. This can be done by using simulations, for which is useful the use of models to recreate the ISM and CGM conditions and study the evolution of the winds.

Based on galactic wind observations, it can be asserted that they are multi-phase flows. Indeed, observations give us information about, very hot, hot, warm, cold and relativistic phases. The very hot one is about $T \sim 10^8$K, and it is unbound from the galactic potential, due to the fact that the temperature is greater than the escape temperature (which quantifies if the wind has enough kinetic energy to escape from the gravitational influence of the galaxy) (see e.g. Heckman & Thompson 2017[38]; Nguyen et al. 2022[39]). The hot phase with $T \sim 10^{6.5}$K has been detected via soft X-ray emission from the galactic winds in starburst galaxies (see Strickland & Stevens 2000[37]; Griffiths & Heckman 1997[40]). The warm phase is mainly seen via spectroscopy in mid-infrared observations. In addition, the cold phase is observed and mapped via spectroscopy in millimeter-wave (see e.g. Heckman & Thompson 2017[38]; Heckman et al. 1990[41]; Beirão et al 2015[42]). Based on these, how can we establish a connection between the formation of superbubbles and galactic winds? It is crucial to comprehend that if a significant portion of the energy released by SNe, which are the primary drivers behind chimney formation as Chevalier & Clegg mentioned in their work in 1985[43]), becomes thermalized*, it results in the generation of a powerful wind that escapes from the region of active star formation. This phenomenon leads to the creation of structures known as superbubbles, and the collection of such bubbles to the formation of coherent, large-scale galactic winds/outflows.

Understanding the importance of bubbles in the formation of galactic winds, it is necessary to analyse how to implement those conditions and phenomena into numerical models. Thus, let us imagine a region of radius R (i.e. assuming a spherical symmetry), where energy is injected in form of kinetic energy and this thermalizes as time passes, thus producing the outflow that escapes from the initial region, where the mass and energy rates of injection are $\dot{M}$ and $\dot{E}$, respectively. Without considering the rotation, gravitational forces and radiative cooling, the hydrodynamic equations (2.2, 2.3, 2.4) for bubble formation are the equations of the Chevalier and Clegg model (CC85) (see Chevalier & Clegg 1985[43]; Heckman & Thompson 2017[38]; Nguyen et al. 2022[39]).

$$\frac{1}{r^2}\frac{d}{dr}(\rho v r^2) = q, \tag{2.2}$$

$$v\frac{dv}{dr} = -\frac{1}{\rho}\frac{dP}{dr} - \frac{qv}{\rho}, \tag{2.3}$$

$$\frac{1}{r^2}\frac{d}{dr}\left[\rho v r^2\left(\frac{1}{2}v^2 + \frac{\gamma}{\gamma-1}\frac{P}{\rho}\right)\right] = Q, \tag{2.4}$$

Here, r represents the radial coordinate, ρ denotes the density, v is the wind velocity, γ stands for the adiabatic index, and P is the pressure. According to Heckman & Thompson 2017[38]:

---

*Process by which a system reaches a thermal equilibrium with its environment.

$$q = \begin{cases} \frac{\dot{M}}{V} & \text{if } r \leq R \\ 0 & \text{if } r > R \end{cases} \quad \text{and} \quad Q = \begin{cases} \frac{\dot{E}}{V} & \text{if } r \leq R \\ 0 & \text{if } r > R \end{cases} \tag{2.5}$$

Where V is the volume of the sphere of radius R. It is possible to scale the energy injection rate as follows; $\dot{E} = \alpha \dot{E}_{SN}$, here α is the thermalization efficiency, and $\dot{E}_{SN}$ is the energy expected from one SN. Furthermore, it is also possible to scale the mass injection rate $\dot{M} = \beta \text{SFR}$, where SFR accounts for SF rate (see e.g. Heckman & Thompson 2017[38]), and β is a factor that is related to mass loading and can help account for possible cooling (see Chevalier & Clegg 1985[43]). In our numerical models, $\dot{E}$ and $\dot{M}$ are fixed quantities, which we use to inject energy and mass into the ISM disc (see details in the next sections).

After some approximations we get an expression that relates the momentum injection rate with the bolometric luminosity (L) and the speed of light (c):

$$\dot{P} \simeq 5(\alpha\beta)^{\frac{1}{2}} \frac{L}{c} \tag{2.6}$$

This relationship is significant because it allows us to determine the factors α and β based on X-ray observations (see Heckman & Thompson 2017[38]), which is important because we can estimate the rate of injection in energy or in mass in order to recreate a SF-feedback scenario via numerical simulations.

Hot winds have been investigated by several research groups, according to Heckman & Thompson 2017[38] the idea of matter and energy injections at large scales is more realistic, so that is the idea we pursue in our investigation, i.e. to inject energy and mass in order to get a simulation of the SF zone in star-forming systems, e.g. M82 or the nuclear wind in our Galaxy.

2.1.4 Gravitational field

According to Cooper, et al. 2008[24], the gravitational potential has two principal components, one related with the disc and the other one with the stellar spheroid. Thus the total gravitational potential is the sum of both terms ($\Phi_{tot} = \Phi_{spheroid} + \Phi_{disc}$). The equations are described as follows:

$$\Phi_{disc}(r, z) = -\frac{GM_{disc}}{\sqrt{r^2 + \left(a + \sqrt{z^2 + b^2}\right)^2}} \tag{2.7}$$

$$\Phi_{spheroid}(R) = -\frac{GM_{ss}}{r_0} \left\{ \frac{ln\left[(R/r_0) + \sqrt{1 + (R/r_0)^2}\right]}{(R/r_0)} \right\} \tag{2.8}$$

Where $R = \left(r^2 + z^2\right)^{1/2}$ is the radius of the spheroid, M_{ss} and M_{disc} are the masses of the spheroid and the disc, respectively, r_0 is the core radius, and a and b are the radial and vertical scale length and height, respectively.

As part of this thesis, we implemented this gravitational potential in Python, with the objective of determining if the equations 2.7 and 2.8 are correct based on the parameters given by Sofue Y. 1998[2], thus obtaining the same rotation curve as in their paper for M82 (see Fig 2.2). This velocity is crucial in our numerical modelling to prevent all the gas from gravitationally collapsing into a central point, and also to attain a realistic structure by angular momentum conservation.
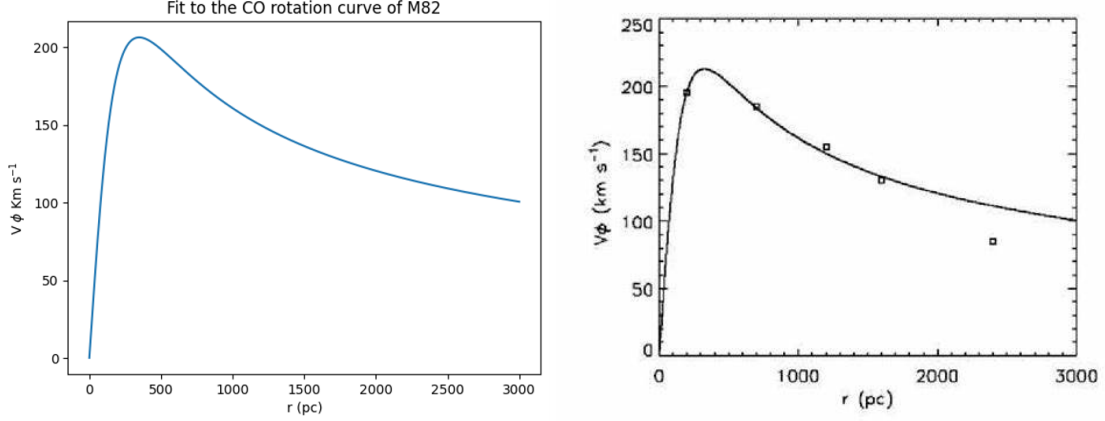
Figure 2.2: Rotation curve of the M82 galaxy based on equations of gravitational potential for a spiral galaxy and plotted with our python routines (left). For comparison with the literature, we show the same curve, as reported in Sofue Y. 1998[2]. (Right)

2.1.5   Density field

Once the gravitational potential of the model is established, it is necessary to implement the CGM and ISM stratified atmosphere. With our python routines, previously used for the implementation of the potential, we could establish the relation between the potential and the distribution of density in two important regions, namely the halo and the disc. The resulting density field are shown by Strickland & Stevens 2000[37]. For the CGM halo, we have:

$$\frac{\rho_{\text{halo}}(r,z)}{\rho_{\text{halo}}(0,0)} = \exp\left[-\frac{\Phi_{\text{tot}}(r,z) - e_{\text{h}}^2\Phi_{\text{tot}}(r,0) - (1 - e_{\text{h}}^2)\Phi_{\text{tot}}(0,0)}{c_{\text{s,h}}^2}\right] \tag{2.9}$$

where, the isothermal sound speed is $c_{\text{s,h}}^2 = (kT_{\text{h}}/\mu m)^{1/2}$ and the ratio of the azimuthal and Keplerian velocity is e_{h}, which for our purposes is zero, because we implement a non-rotating halo. For the disc, we have:

$$\frac{\rho_{\text{disc}}(r,z)}{\rho_{\text{disc}}(0,0)} = \exp\left[-\frac{\Phi_{\text{tot}}(r,z) - e_{\text{d}}^2\Phi_{\text{tot}}(r,0) - (1 - e_{\text{d}}^2)\Phi_{\text{tot}}(0,0)}{\sigma_{\text{t}}^2 + c_{\text{s,d}}^2}\right] \tag{2.10}$$

where, the warm gas sound speed is $c_{\text{s,d}}^2 = (kT_{\text{d}}/\mu m)^{1/2}$, σ_{t} is a factor controlling the strength of the turbulent dispersion velocity of the clouds, and e_{d} is the ratio of velocities, (in this case we use a value of 0.95 because we need a gaseous disc in all models).

The fractal clouds were generated based on lognormal density fields following the same steps as Banda-Barragán et al. 2019[44] reported. First, the outside regions in the domain of the clouds were masked (i.e. the regions outside a specific radius). Second, the average density was scaled to an specific value (ρ_{cloud}). Third, the data was interpolated into a 3D domain bounded by the density equations 2.9, and 2.10. The interpolation range is variable and it is

described in the following chapters. The simulations with the fractal clouds generated above are computationally expensive, thus restricting the resolution values of the simulations (see e.g. Banda-Barragán et al. 2019[44]).

With the above equations, the stratified atmospheres were established for three different models with a distinct value of σ_t, those models are shown in Fig 2.3.
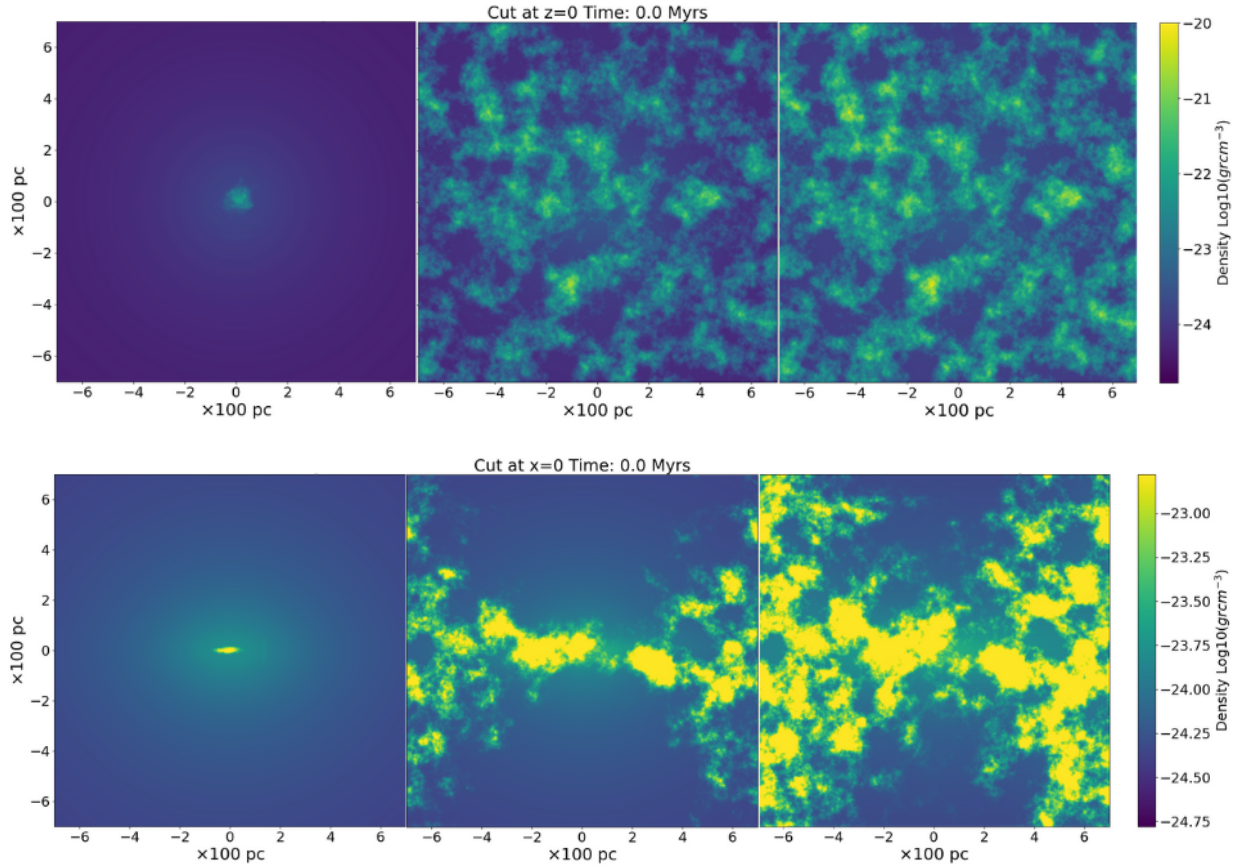
Figure 2.3: Top images: Cross-section at $z = 0$ of the grid for different fractal density fields. This provides a top-down view of the ISM disc. Bottom images: Cross-section at $x = 0$ of the grid reveals stratified atmospheres, which provides an edge-on view of the ISM disc and CGM halo.. Images in each column correspond to the same σ_t value, while keeping all other parameters constant in equations 2.10 and 2.9 (see the parameters in Table 3.1). Displayed from left to right: $\sigma_t = 0$ km/s, 60 km/s, and 100 km/s.

Chapter 3

Methodology & Numerical Modelling

3.1 PLUTO

PLUTO is a free and open-source software, created by Mignone et al. (2007)[45]. It contains a package of numerical solvers, which are useful to simulate the dynamics of astrophysical gases. The code solves partial differential equations, which could be parabolic or hyperbolic. The requirements of PLUTO for running a simulation are: Python (which is used as a wrapper) and a C compiler, because it is written in C language. Furthermore, the parallelization is managed inside the environment (i.e. it is not necessary an external package apart from the compiler itself). It uses the Message Passing Interface (MPI) for parallelization. Moreover, hydrodynamical simulations of blasts, jets, disc vortices, stellar winds, etc., are some sample test configurations that PLUTO includes as a "Test Problems". Such codes can be used as the basis for own customised simulations by adding different initial conditions and numerical setups as in this project. The PLUTO code is flexible enough to deal with different initial conditions and solvers and offers a variety of numerical algorithms based on Godunov-type schemes.

3.2 Python

Python is a free, open-source, high-level programming language used in scientific visualization and data analysis. For this thesis, python was useful for reading and analyzing several datasets of simulations performed in PLUTO. The scripts that python allows us to create were also useful for High-Performance Computing (HPC) facilities, where it is necessary to upload and submit the scripts as compute jobs, with the aim of obtaining all the files of visualization and analysis. Python scripts were also practical because of their repeatability, as the scripts were used in several disc-wind models, thus optimising data analysis time. With the use of python software and python-based visualization packages, such as VisIt* (see Childs et al. 2012[46]), we could generate high-quality plots and movies of the simulations, which provide us with important features of the dynamics of the gas under the applied conditions.

---

*https://visit-dav.github.io/visit-website/index.html

3.3   Disc-wind Simulations

All the simulations performed for this thesis were carried out by using the PLUTO code (see Mignone et al. 2007[45]). Our simulations in PLUTO are centered on a thermally ideal gas described by the following equation of state (EOS), see equation 3.1.

$$p = nk_BT = \frac{\rho}{m_u\mu}k_BT \tag{3.1}$$

where, p is the thermal pressure, n is the total particle number density, k_B is the Boltzmann constant, T is the temperature, ρ is the density, m_u is the atomic mass unit, and μ is the mean particle mass. Equation 3.1 can also be written as shown below, i.e., in a manner that describes the internal energy of a calorically ideal gas, where the value of the polytropic index γ is fixed at 5/3 for the three models.

$$\rho\varepsilon = \frac{p}{\gamma - 1} \tag{3.2}$$

Furthermore, the HydroDynamics (HD) module of PLUTO was used to solve the Euler equation of fluid dynamics for an adiabatic gas. Simulations include three dimensional Cartesian system ([X,Y,Z]). As the simulation progresses, PLUTO solves the following conservation laws:

$$\frac{\partial}{\partial t}\begin{pmatrix} \rho \\ \mathbf{m} \\ E_t + \rho\Phi \end{pmatrix} + \Delta \cdot \begin{pmatrix} \rho\mathbf{v} \\ \mathbf{mv} + p\mathbf{l} \\ (E_t + p + \rho\Phi)\mathbf{v} \end{pmatrix}^T = \begin{pmatrix} 0 \\ -\rho\Delta\Phi + \rho\mathbf{g} \\ \mathbf{m} \cdot \mathbf{g} \end{pmatrix} \tag{3.3}$$

where ρ is the mass density, $\mathbf{v}$ is the velocity, $\mathbf{m}$ is the momentum density defined as follows $\mathbf{m} = \rho\,\mathbf{v}$, E_t (composed by kinetic energy k and internal energy ε) is the total energy density, p is the thermal pressure, and Φ is the gravitational potential.

In addition, our numerical setup specifies a linear order of integration for the spatial reconstruction in a finite-volume scheme. In this process, the fluid variables undergo a Total Variation Diminishing (TVD) reconstruction, which allows conservation as the flow moves across the computational domain with 2nd order of accuracy in space. To achieve high accuracy while considering computational costs, a third-order Runge-Kutta method (RK3) was used in the models for time stepping. The combination of a linear spatial reconstruction and a RK3 time-marching scheme give us a better stability for a limit value of the Courant-Friedrichs-Lewy (CFL) number CFL $\lesssim \frac{1}{N_{\mathrm{dim}}}$, where N_{dim} is the number of dimensions (see Mignone et al. 2007[45]). In our 3D simulations, therefore the CFL value is set to 0.33 for all the models. Besides, the PLUTO code was configured for the three models with a Harten, Lax, Van Leer approximate Riemann Solver (HLLC), which is used for computing solutions using characteristics (see Toro 2019[47]). The HLLC solver reduces numerical dissipation, which is helpful for our simulations because it provides a better representation of the gas flowing throughout the computational domain. This improvement proves valuable for observing the outflows and also the formation of superbubbles.

Moreover, our numerical code used tri-linear interpolation for prescribing the fractal cloud based on two input files (rho0.dbl and grid0.dbl), which helped us to implement a turbulent ISM disc (see section 2.1.5) in the computational domain , which as we mention below, aids the formation of superbubbles as it facilitates the motion of the gas along the vertical axis.

3.4 Initial and Boundary Conditions

Our investigation is centered in studying the formation of superbubbles in the Galactic Center. Thus our model includes the gravitational potential of the Galaxy, which was implemented in the code using the total gravitational potential, which is the sum of equations 2.7 and 2.8. Furthermore, a distribution of density is necessary to re-create the initial conditions as a stratified atmosphere of a galaxy. Such density distribution is based on equations 2.9 and 2.10, so as part of this thesis, we implemented them into PLUTO code.

Table 3.1: Initial conditions of our disc-wind simulations, based on observationally-constrained data for the Milky Way. The first and second columns indicate the parameter name and notation, respectively. The third column indicates the value of each parameter in the respective units shown in parenthesis.

Parameter	Symbol	Value
disc mass	M_{disc}	1.0×10^{10} ($M_\odot$)
Spheroid mass	M_{ss}	9.0×10^{9} ($M_\odot$)
Core radius	r_0	250 (pc)
Radial scale length	a	150 (pc)
Vertical scale length	b	50 (pc)
Central halo density	n_{h}	0.1 (cm^{-3})
Average disc density	$n_{\text{d,avg}}$	100 (cm^{-3})
Halo temperature	T_{h}	5.00×10^{6} (K)
Average disc temperature	$T_{\text{d,avg}}$	1.00×10^{4} (K)
Star formation zone radius	r_{sf}	150 (pc)
Star formation zone height	h_{sf}	40 (pc)
Mass injection rate	$\dot{M}$	0.1 ($M_\odot \text{yr}^{-1}$)
Energy injection rate	$\dot{E}$	1×10^{42} (erg s^{-1})
Spatial range	SR	1400×1400×1400 (pc^3)

Additionally, it is important to consider the rotation of the initial distribution of the clouds. This physical parameter plays an important role in impeding the rapid collapse of gas towards the center. Thus, the rotation velocity, defined by Strickland & Stevens 2000[37], is the following:

$$v_\Phi = e_{\text{rot}} \left(r \frac{\partial \Phi_{\text{tot}}}{\partial r} \right)^{1/2} \tag{3.4}$$

where, $e_{\text{rot}} = 1$ for a complete disc supported by rotation.

The velocity condition implemented in the model is described by equation 3.4, taking into account the angle in the *xy* plane, where $\theta = \arctan\left(\frac{y}{x}\right)$.

$$v_x = \begin{cases} 0 & \text{if } x = y = 0 \\ v_\Phi \cos(\theta + \frac{\pi}{2}) & \text{if } x > 0 \\ v_\Phi \cos(\theta + \frac{3\pi}{2}) & \text{if } x < 0 \end{cases} \quad , \quad v_y = \begin{cases} 0 & \text{if } x = y = 0 \\ v_\Phi \sin(\theta + \frac{\pi}{2}) & \text{if } x > 0 \\ v_\Phi \sin(\theta + \frac{3\pi}{2}) & \text{if } x < 0 \end{cases} \quad , \quad v_z = 0 \quad \forall x \qquad (3.5)$$

Moreover, it is important to say that thermal pressure is constant in all the computational meshing for all the models. Also, all the initial parameters needed to calculate the gravitational potential, the distribution of density and the rotational velocity are in Table 3.1.

The computational mesh is a cube with (1:1:1) aspect ratio, and it is oriented within a Cartesian coordinate system denoted as (X, Y, Z). As a consequence of the rotational velocity, some of the gas that comes out of the computational domain can potentially return. In order to prevent gas returning into the computational domain, we implemented diode boundary conditions (equation 3.6) to the ghost zones at the beginning ($X_{n,\text{beg}}$) and end ($X_{n,\text{end}}$) of the physical domain, where n goes from 1 to 3. Periodic boundary conditions, in this case, does not represent such a realistic condition to the model, so they would affect the results of our analysis.

$$\begin{cases} v_{X_{n,\text{beg}}} & \rightarrow Min[v_{X_{n,\text{beg}}}] \\ v_{X_{n,\text{end}}} & \rightarrow Max[v_{X_{n,\text{end}}}] \end{cases} \qquad (3.6)$$

Here, $v_{X_{n,\text{beg}}}$ represents the velocities at the beginning ghost zones. To prevent the inflow of matter, any gas exiting the computational domain on the starting side of (X,Y,Z) with a specific velocity is adjusted to the minimum velocity among all beginning sides ($Min[v_{X_{n,\text{beg}}}]$). This adjustment ensures that there is no reintroduction of gas into the computational grid. On the other hand, $v_{X_{n,\text{end}}}$ denotes the velocities at the end. In this scenario, the velocity of the outgoing gas is set to the maximum velocity of each end side in X, Y, and Z ($Max[v_{X_{n,\text{end}}}]$). This prevents gas from re-entering the computational domain.

Once the equations 3.5 and 3.6 were established in the model, we obtain the 3D velocity field shown with arrows in Fig 3.1.

3.5   Diagnostics

With the aim of understanding the formation and evolution of Galactic superbubbles, various diagnostics are required from the data obtained through simulations. The total mass in the simulation, represented by the variable M, is calculated as follows:

$$M = \int \rho \, dV \qquad (3.7)$$

where ρ is the density, and V is the volume. The kinetic energy is calculated by:

$$k = \frac{1}{2} \int \rho \, |\mathbf{v}|^2 dV \qquad (3.8)$$
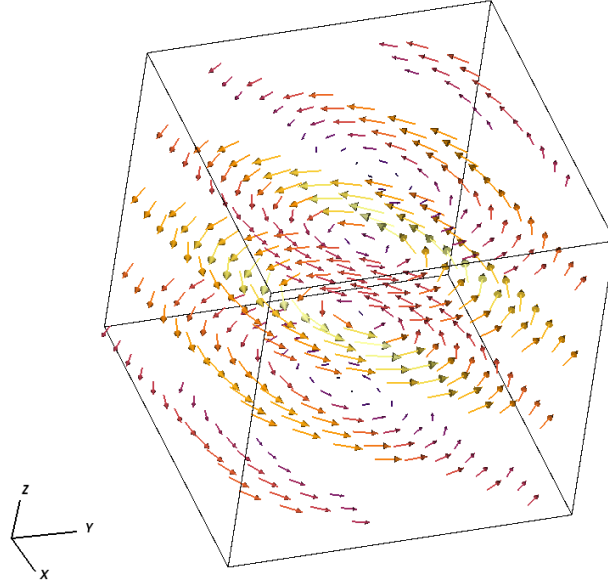
Figure 3.1: Three-dimensional depiction of velocity distribution: This representation illustrates the velocity field within the computational domain, with arrows indicating the direction of the velocity and the colour representing the speed.

here, $|\mathbf{v}|$ is the modulus of the velocity. In a similar manner, the internal energy was calculated by the use of the ideal equation of state 3.2, and the total energy is computed as the sum of both the kinetic energy (k) and the internal energy (ε).

For the study of phase diagrams, the number density n was defined as follows:

$$n = \frac{\rho}{\mu \, m_u} \tag{3.9}$$

where, μ is the mean particle mass, which is set to 0.67 for all the simulations, and m is the atomic mass unit. Additionally, the temperature was calculated using the EOS 3.1, for the analysis diagnostics of phase diagrams.

3.5.1 Mass and energy injection recipe

The main motivation for our numerical models is studying the GC outflow in out Galaxy, which involves modelling the region where SF occurs. As mentioned in Chapters 1 and 2, this SF region is an active zone with various processes such as supernovae and star formation. To replicate these conditions, and considering the small size of individual SN and protostars compared to the resolution of our computational domain and the difficulty of simulating these phenomena one by one, we purpose the implementation of an injection zone (the SF region). The concept is to mimic SF feedback by injecting mass and energy continuously as the simulation is evolving in a cylindrical zone with height h_{sf} and radius r_{sf}, whose values are in Table 3.1. For a realistic recipe, our injection is proportional to

the concentration of gas (i.e. to the gas density), and based on observed parameters of mass and energy injection in the Milky Way.

The mass injection was implemented following Cooper et al. 2008[24] as:

$$\frac{dM}{dt\,dV} = \frac{\dot{M}\rho}{\int \rho\,dV} \tag{3.10}$$

where M is the mass and $\dot{M}$ is the mass injection rate, whose value is shown in Table 3.1.

Likewise, the energy injection was established following the equation detailed by Cooper et al 2008[24]:

$$\frac{dE}{dt\,dV} = \frac{\dot{E}\rho}{\int \rho\,dV} \tag{3.11}$$

where, E is the energy and $\dot{E}$ is the energy injection rate, whose value is shown in Table 3.1. The integration on the right hand side of both equations (3.10 and 3.11) is over the volume of the SF region. However, in the PLUTO code we needed to implement an injection based on thermal pressure, We develop the following expression from equation 3.11 and also with the use of equation 3.2:

$$\frac{dP}{dt\,dV} = \frac{\dot{E}\rho^2(\gamma - 1)}{\left(\int \rho\,dV\right)^2} \tag{3.12}$$

After providing a detailed overview of the code methodology, three models were simulated with distinct ISM distributions to investigate the formation of galactic superbubbles for different turbulent density ISM distributions. Each model has a resolution of $320 \times 320 \times 320$ for high-resolution, $160 \times 160 \times 160$ for half-resolution, and $80 \times 80 \times 80$ for low-resolution, with variable being σ_t which is the only factor changing across the models (see Table 3.2).

Table 3.2: Simulation parameters of the three main models with different distribution of the ISM

Model	Resolution	σ_t (km s^{-1})	Thermodynamic type	Spatial Range (pc^3)
M1	320×320×320	0	Adiabatic	1400×1400×1400
M2	320×320×320	60	Adiabatic	1400×1400×1400
M3	320×320×320	100	Adiabatic	1400×1400×1400
Half-resolution	160×160×160	60	Adiabatic	1400×1400×1400
Low-resolution	80×80×80	60	Adiabatic	1400×1400×1400

This chapter provided sufficient information and computational tools for conducting simulations on the formation and evolution of superbubbles. The next chapter shows the results of these simulations, with a thorough discussion and analysis of the outcomes.

Chapter 4

Results & Discussion

4.1 Evolution of the Superbubbles

With the aim of studying the formation of galactic superbubbles with our numerical disc-wind models, two-dimensional cross sections of the 3D cubes were created for $x = 0$ and $z = 0$ (see Fig. 4.1 and Fig. 4.2, respectively). Those figures show density maps of the three models, $\sigma_t = 0$, 60, 100 km s^{-1}, at various times, with the evolution progressing from the top to the bottom over a span of 4.89 Myr. The choice of different values for σ_t is introduced as it is necessary to identify how the gas distribution affects the formation of outflows from the Galactic center vertically (i.e. on the z-axis). The evolution of the three models can be illustrated with two different cross section, one for the $x = 0$ cross section (Fig. 4.1), and the other for the $z = 0$ cross section (Fig. 4.2).

First, Figure 4.1 shows the evolution of the simulation. At $t = 0$, it is possible to see the different initial distributions of the gas controlled by the σ_t parameter. Larger values of this parameter lead to ticker ISM discs, and vice versa. At $t = 0.977$ Myr, there is an increase of density in the SF region, and also, the overall morphology of the gas in the central region is different. There exist pressure gradients in the medium, which can lead to inflow of high-latitude gas onto the Galactic plane. This is more obvious in the M2 and M3 models, where the gas falls towards the center due to the gravitational potential.

At $t = 1.96$ Myr, outflows begin to appear in all three models, reaching almost 200 pc along the vertical axis. Also is possible to notice, an increase in density and pressure. At that time, the disc, in the three models, becomes much thicker, due to the injection of material in the Galactic Center via supernova explosions. At $t = 2.93$ Myr, the gas, in M1 and M2, expands laterally due to rotation, while in the M3, the expansion in the y-axis is not so considerable. This occurs because the concentration of material on the lateral shafts prevents gas from escaping to the sides. In contrast, it is possible to see how the expansion in M1 towards the laterals is uniform compared with M2 and M3. Furthermore, the expansion along the z-axis reaches greater height in M3, even when the gravitational attraction leads to further inflow of gas onto the Galactic plane in this model. Due to the same effect, we can see some filaments of gas of around 10^{-23} g cm^{-3} falling towards the center.

At $t = 3.91$ Myr after the start of the inflow process, the gas has been falling towards the center of the galaxy
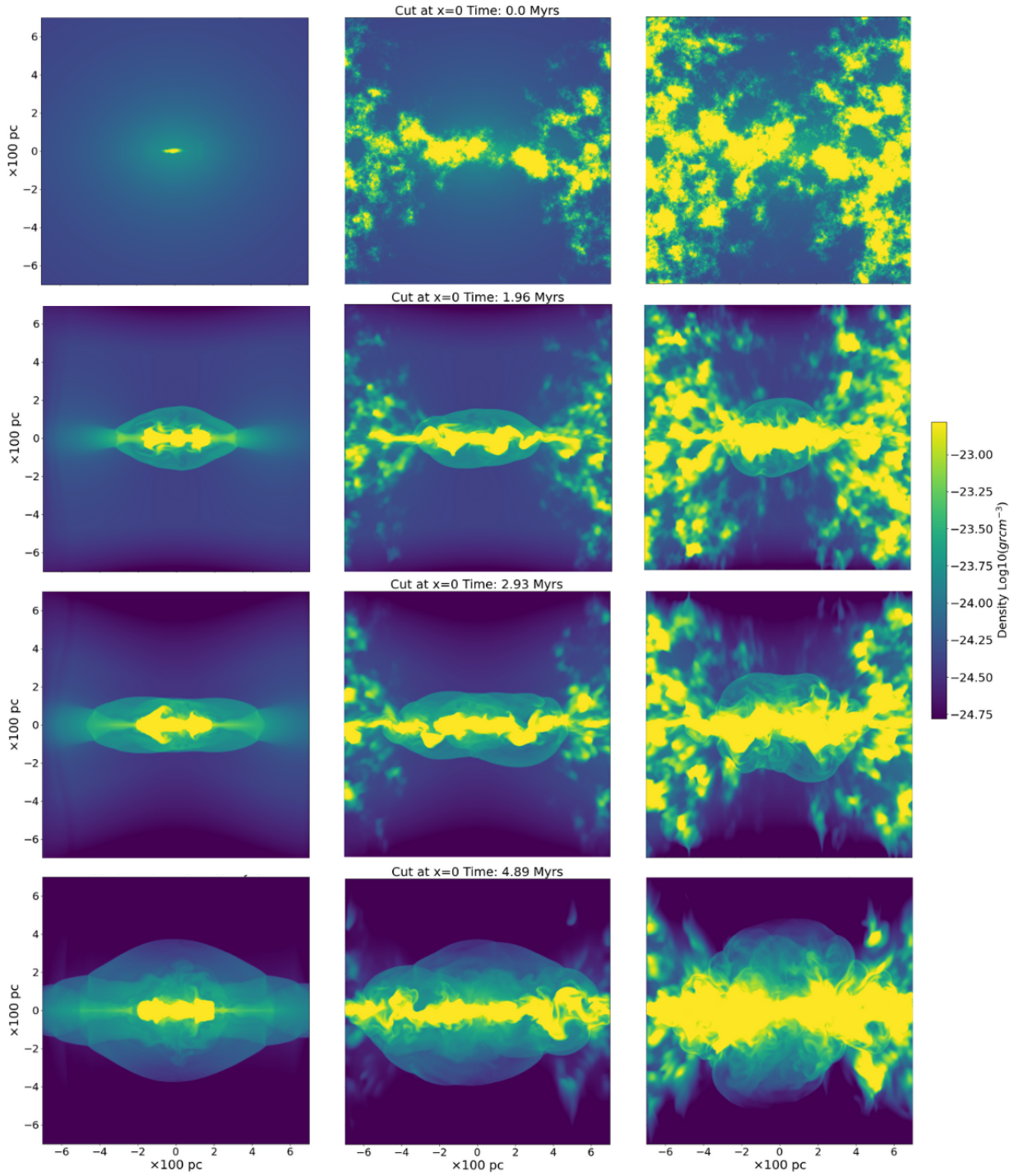
Figure 4.1: Evolution of superbubbles depicted along the $x = 0$ axis cross-section over a 4.89-million-year period for all three models. From left to right there is an increase in σ_t from $0\,\mathrm{km\,s^{-1}}$ through $60\,\mathrm{km\,s^{-1}}$ and to $100\,\mathrm{km\,s^{-1}}$. From top to bottom: the evolution shows the dynamical progression in the representation for each model.

with more impact in the center, as can be seen at late times in the Fig. 4.1. Moreover, the bubbles of M3 model that are in formation merge and have reached a considerable vertical height of between 300 pc and 400 pc, exceeding by a few parsecs the height reached by the bubbles in M2. Finally, at the end of the simulation at $t = 4.89$ Myr, we can see how some bubbles have merged, and so producing superbubbles. Furthermore, because of the lower densities in the vertical direction above and below the disc, the outflowing gas can reach a larger distance from the disc (i.e. on the vertical axis), the gas has reached a higher latitude in all models.

In Figure 4.2, we show density slices for $z = 0$ of the same simulation for our three models. First, it is possible to see the initial distribution of density for a time t=0 Myr. By 0.997 Myr, we can see the effect of the rotational velocity, and the rearrangement of the gas due to that factor. It can also be seen how the density increases for all three models in the defined SF region. For later times until reaching $t = 4.89$ Myr, we can observe how in the M1 model, there is not a high-density disc. We can only see a disc of less dense gas, it could be related with low surface brightness galaxies. On the other hand, for the models M2 and M3, we can see the disc formation, in the same manner along the years for the two models. We can also see the increment in density in the center. By the action of rotation and pressure gradients arising from the SF region the density grows also in the outside regions.

Furthermore, the images reveal an equilibrium between gravitational attraction and rotational forces, because as it is possible to see the gas does not collapse to the center under the gravitational potential, but it is rather maintained in a disc. This phenomenon can be attributed to its sustained motion, facilitated by the rotational velocity. In a general way, the evolution shows how the outflows are formed due to the ejection of material from the center, so the bubbles arise, merge with others, and reach heights of hundred of parsecs.

4.2 The Role of the Turbulence σ_t Parameter

In Fig. 4.1 from $t = 1.96$ Myr onward, it is noticeable how the scale height of the disc varies for each model. The sole parameter changing between simulations is the initial turbulence parameter (i.e., σ_t), which controls the scale height of the disc, i.e. its vertical extent. This correlation is also evident in Fig. 4.2, where an increase in σ_t corresponds to an elevated disc height. Specially, it can be observed how the disc for the M3 model is higher in comparison with the M2 model, and both discs of models M2 and M3 are considerably thicker than the disc of model M1. These differences are indicative of how the turbulence parameter produces significant variations in disc formation and densities.

Although the turbulence parameter is closely related to the scale height of the disc, there are also implications for the gas density. The variation in the average density along the simulation time can be observed in the Fig. 4.3, where the morphology of the evolving gas also varies throughout the entire time. In addition, we also plot the standard deviation for the three models.

Fig. 4.3 reveals that the average gas density covers ranges typically on the order of $\sim (10^{-24} - 10^{-23})$g cm^{-3}, we have three lines that represent the three models. In the case of $\sigma_t = 0$ and 60 km/s, a linear increase in the average density is evident, with only differences in magnitude between the models. This discrepancy can be attributed to the presence of more ISM gas in the initial atmosphere of model M2 (orange line). On the other hand, in model M3 (green line), it is possible to see a drop in the average density over mos of the simulation time, reaching its minimum
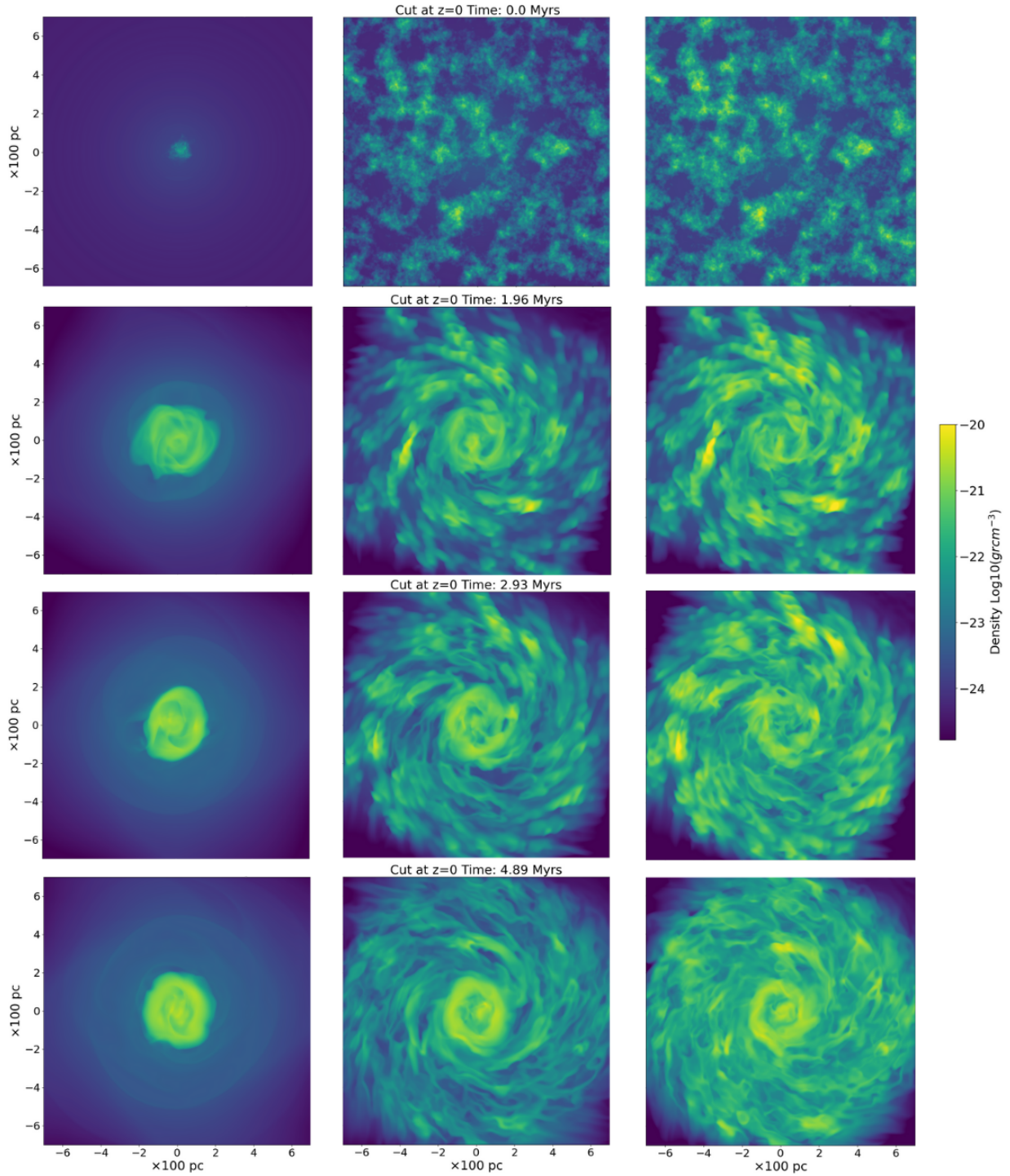
Figure 4.2: Density map of the evolution of superbubbles depicted along the $z = 0$ axis cross-section over a 4.89-million-year period for all three models. From left to right there is the change in σ_t for $0\,\mathrm{km\,s^{-1}}$ to $100\,\mathrm{km\,s^{-1}}$. From top to bottom: the evolution shows the dynamical progression in the representation for each model.
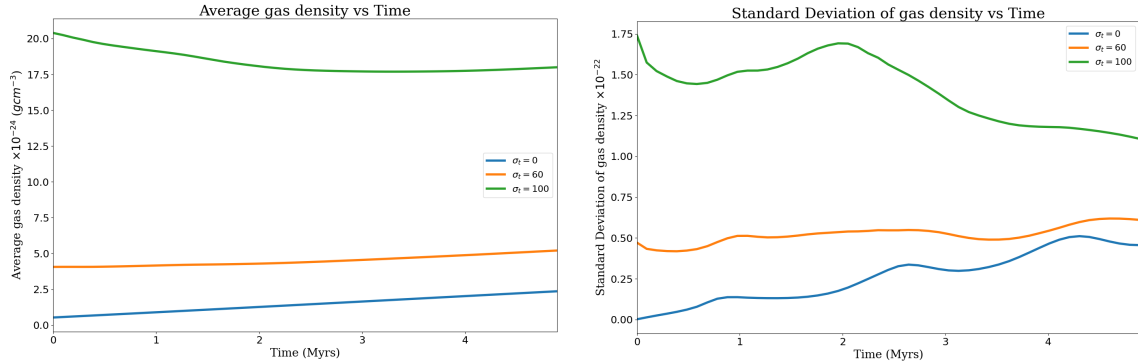
Figure 4.3: Time evolution of the total average density (left) and the standard deviation of the density (right) over the 4.89 millions of years, for the three different values of σ_t.

at about 3 Myr, after that time the average density starts to grow for another 1.89 Myr until the end of the simulation time.

In addition, the plot of the standard deviation in the case of $\sigma_\text{t} = 0\,km\,s^{-1}$ (blue line in Fig. 4.3) is variable and shows some periodicity in the increases and decreases of the density standard deviation. Moreover, the deviation is increasing with the passage of time. For the M2 model, the standard deviation seems to be nearly constant as time passes, and the deviation shows certain increases and decreases, which practically coincide with the times of the M1 model. Finally, the $\sigma_\text{t} = 100\,km\,s^{-1}$ model is the only one in which the standard deviation is decaying, with a noticeable increase for a time of about 2 Myr, we can also observe certain increases in the deviation, which are small related to the highest peak of the curve, but which are related to the times in which the deviations, of the two previous models, also have increases.

The tendency in the increase in density throughout the simulation is due to the injection of material by the supernova explosions that are occurring in the central region, this is reflected in the M1 and M2 models and late in the M3 model, but why is there a decrease in the mean density for this model? It occurs because of the implemented rotation and boundary conditions. The gas leaves the computational domain and does not re-enter, so we have mass loss, additionally, due to the shock waves, originated by the central SN explosions, much material is dragged out of the domain.

The variations in the density standard deviation, can be interpreted by the redistribution of the gas in the domain. Namely, the times for which there are some peaks in the curve for all the models ($\sim$ 1 Myr, 2.5 Myr and 4 Myr), are in relation with the increment in the amount of the injection of material and thermal pressure to the media via SN explosions. This happens because, before those times, the gas falls into the central region driving the formation of new stars that will then give rise to hundreds of supernova explosions. Finally, in these models the decrease in the standard deviation is due to the outflow of gas from the edges, propelled by both rotational forces and the thrust generated by the SN explosive events. This clarifies the observed pattern where an initial rise in deviation is succeeded by a subsequent decline.

The thermal gas pressure is another variable in which the value of the turbulence parameter has an impact, the initial distribution in the atmosphere can cause an increment in the injection of thermal pressure to the media, as it is possible to see in Fig. 4.4.
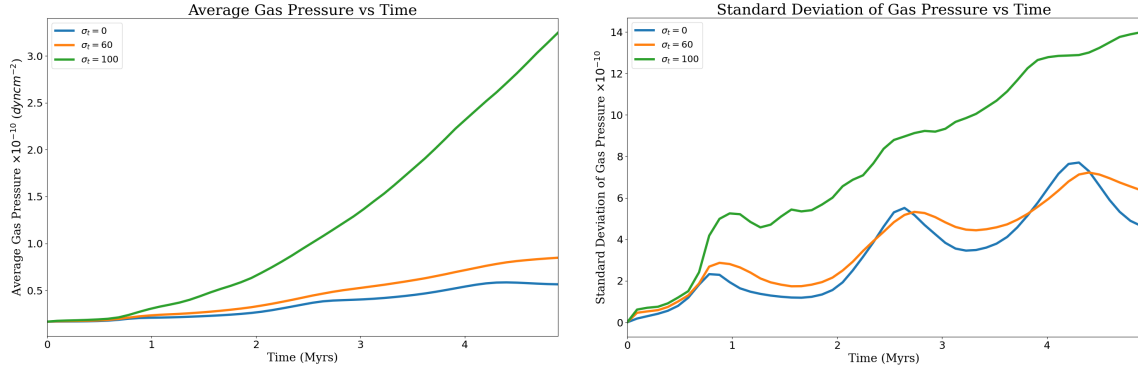

Figure 4.4: Time evolution of the total average pressure (left) and the standard deviation of the pressure (right) over the 4.89 Myr, for the three different values of σ_t

.

On the left hand side of Fig. 4.4 we show the average pressure as a function of simulation time. The ranges for the pressure in the models are on the order of $\sim 10^{-10}$ to $\sim 10^{-11} \mathrm{dyn\,cm^{-2}}$. Each line represents one model, in the case of M1 (blue line), the curve has some periodicity in the increase and decrease of the average pressure with a tendency to increment along the time. Also the pressure in M1 has the smallest magnitude compared to the other two models. For the M2 model (orange line), it is possible to see an increment of the pressure as time passes, and, the curve exhibits less prominent peaks and valleys, which coincide with the times of the peaks for M1. The M3 model shows the most prominent increment in the average pressure throughout all time, it seems to follow an exponential growth.

On the right-hand side of Fig. 4.4, the graph shows the standard deviation of gas pressure over the entire time period. Something interesting to notice is the periodicity in the peaks and valleys of the curves for all the models, at almost the same times. The deviations increase in all models as time progresses, with a higher deviation for the $\sigma_t = 100\,km\,s^{-1}$ model.

It is important to note that, unlike in the density plot, the pressures share the same starting point, this is because a uniform initial atmospheric pressure was defined at the outset. Nevertheless, the increment is different for each model. This occurs because the rate of SF in the central region depends on the concentration of gas, and as consequence the formation of stars, which then eject energy via SN explosions, but this varies in time depending on how much gas is in the SF region. For that reason, the M3 model shows more injection of thermal pressure as it has higher densities in the initial distribution inside the SF region. In contrast, the other two models experience less energy and there is a gradient with increasing σ_t as the M2 model demonstrates increased thermal pressure injection, in comparison with M1 model, due to a greater amount of material.

The periodicity in the pressure standard deviation of the models is related, in the same manner as the density standard deviation, with the emergence of strong star formation episodes, led by gas accumulation in the central region. In the evolution (maps shown in Fig. 4.1) before the gas reaches the times ($\sim$ 1 Myr, 2.5Myr and 4 Myr), it is possible to observe the fall of gas via gravitational attraction, leading to a higher concentration of gas in the central region, giving rise to higher SF rates and consequently to larger energy and mass injection rates. We find that this process repeats itself, resulting in a decrease in the pressure and density standard deviation as the gas redistributes, and a certain amount of gas is lost from the edges. The interplay between SF feedback and gas dynamics then explains the periodicity in the standard deviation curves.

4.3   Energy and Mass Injection

In this section we describe how energy changes with time. This is important as we need to ensure that the total amount of energy and mass injected via SF feedback are in agreement with the observationally-constrained values. The total energy in this case is defined by the sum of kinetic plus internal energy. In Fig. 4.5 we show the different types of energy: kinetic (dashed line), internal (dotted line), and total (solid line) are represented by the three different models, each one with an specific color.

Figure 4.5: Evolution of the logarithm of the total, kinetic, and internal energy over a span of 4.89 million years, and depicted for three distinct values of σ_t.

.

Fig. 4.5 shows the difference in energies for each model. The most energetic is the M3 model with energies of the order of $\sim 3.16 \times 10^{56}$erg, followed by the M2 model with energy orders of $\sim 5.62 \times 10^{55}$erg, and finally the M1 model with maximum energies of $\sim 1.99 \times 10^{55}$erg. An important observation to make is that the major contribution

to the total energy in each model is the kinetic energy, while, internal energy playing a lesser role. The total energy for M2 and M3 shows a linear growth, with a non-steep slope, over time, while in the model with $\sigma_t = 0$, it can be seen that the growth appears to be logarithmic in shape, but the magnitude in comparison with the other two models is not so strong.

Due to the intense star formation in the Galactic Center, the energy is constantly in change. In this case, the contribution of the rotational disc, the motion of the gas via pressure of the explosions, the internal energy increment and gravitational collapse, cause the energy to increase over time. The increase in energy over the time span of the simulation (i.e. the slope of the curve) is higher in the M1 model as shown in Fig. 4.5. This occurs due to the fact that the SF zone is surrounded by gas of much lower density compared to the M2 and M3 models, so the kinetic energy is not counteracted and the hot gas produced by the supernovae moves more freely, thus acquiring a higher kinetic energy.

The change in the internal energy is also important to analyze in detail, because it provides information about the injection of mass and energy in form of thermal pressure, as we have implemented in these models. Figure 4.6 shows the change of the logarithm of internal energy in time for our three models.
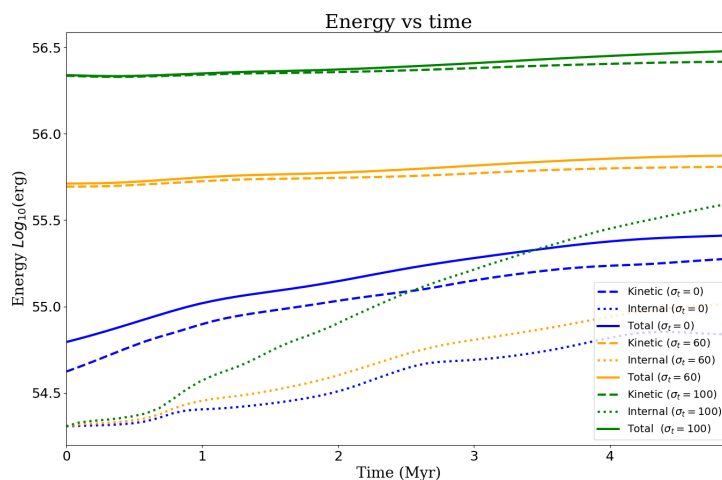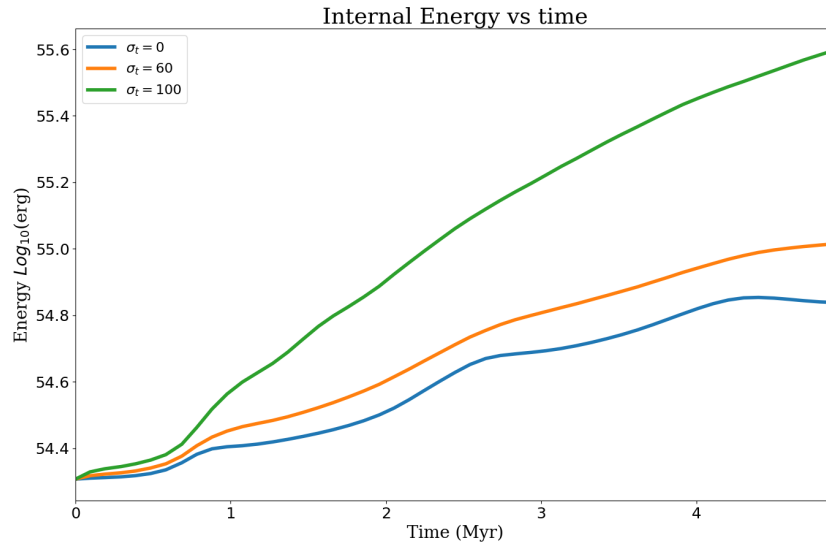

Figure 4.6: Evolution the logarithm of the internal energy over a span of 4.89 million years are depicted for three distinct values of σ_t.

.

Internal energy increases all the models, where the total internal energies go from smallest to largest for models M1, M2 and M3, respectively. Furthermore, it is remarkable how there are certain periodicities in the curves of $\sigma_t = 0$ and $60\,\mathrm{km\,s^{-1}}$, exactly for the same times where we had periodicity in Figs. 4.3 and 4.4. The initial point is

the same in all the three models, because of the uniform initial pressure. Then, there is an abrupt increase before 1 Myr. The internal energy in all the models continues increasing in magnitude, but in the case of the M3 model, the curve is increasing until the end of the simulation, however, in the two remaining models the curve seems to flatten for M2, and decline for M1, towards the end, which could also be just one of the fluctuations. This is indicating the initiation of a new strong SF period, as reflected in the recorded trends across the curves.

The abrupt increment in the internal energy before 1 Myr, and also the periodic increments in the internal energy in the M1 and M2 models, are caused by SN injections and the stellar winds of the supermassive stars, which can heat the surrounding environment. In addition, the increase may be due to the impact of shock waves produced by supernovae, which can compress the gas an heat it up. Moreover, the decreases in the curves, specially for M1 and M2 models, are related with the expansion of the gas from the center, because as the gas gains altitude it loses energy and cools down adiabatically. The fact that the gas in the M3 model does not have periods of internal energy loss is because the magnitude in which the energy decreases is exceeded by the internal energy gained by the gas via strong SF feedback, due to several factors already mentioned. The gas with high values of σ_t is also highly dissipative, in other words the gas could increase its internal energy from e.g. turbulent dissipative processes.
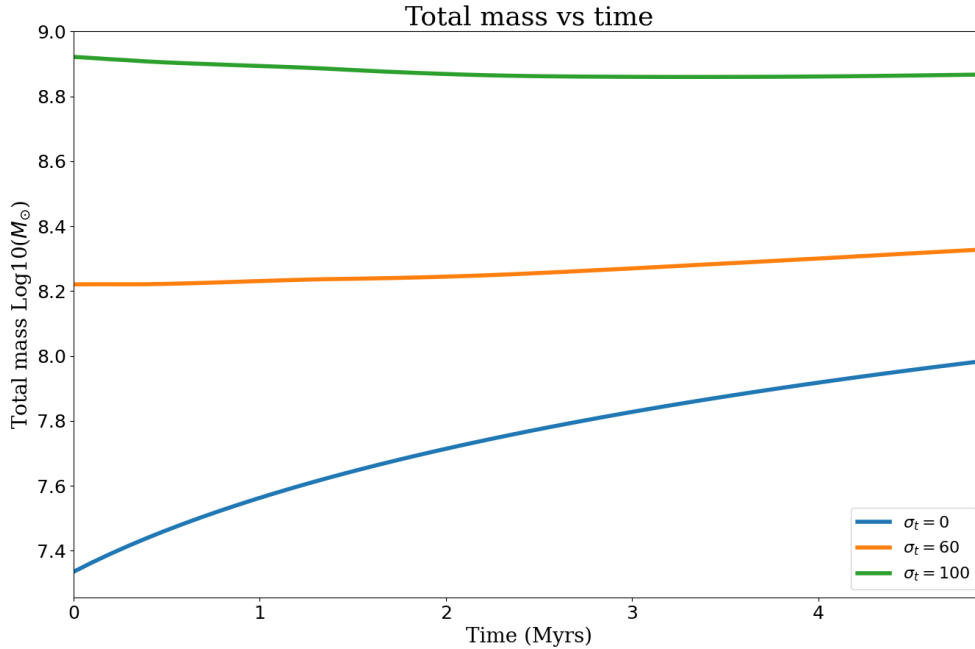

Figure 4.7: Evolution of the logarithm of the total mass in all period of time are depicted for three distinct values of σ_t.

.

In addition, just as the turbulence parameter influences the total density in our models, it similarly affects the total mass content in the computational domain. Figure 4.7 shows the logarithmic curves of mass evolution over

time, with the curve for $\sigma_t = 0\,\mathrm{km\,s^{-1}}$ exhibiting a more pronounced increase, even if its maximum magnitude reach is smaller compared to the other two models. Moreover, it is possible to observe a linear increase in mass for the M2 model, however, the increment is not of considerable magnitude. For the third model, the curve starts with a decrease in magnitude, and around 2.5 Myr it starts to increase, but the increase is not as significant as in the M1 model.

The observed trends in the curves can be attributed to the factors mentioned in the analysis of Figure 4.3. In the M2 and M3 models the increase is not significant as in the curve of the M1 model. The reason for this lies in the gas loss occurring at the boundaries, because a greater central pressure, propagating radially, expels gas from the computational domain. As a result, the injection of mass only slightly exceeds the loss of mass, thus resulting in a relatively small growth of the curve. On the other hand, in the M1 model, the mass generated by the SF zone is much larger than the gas loss at the edges since the gas in the outer regions is much less dense, thus the curve increases over time.

In a nutshell, the turbulence parameter (σ_t), in addition to controlling the scale height of the disc, has a significant influence in some magnitudes, such as the density, mass, pressure, and energy. This parameter changes the magnitude of the variables mentioned before, and in general higher values of σ_t lead to higher absolute values of all these parameters, but the rate of their change with time varies widely and low σ_t values lead to more pronounced slopes.

4.4 Kinematics of Superbubbles

Figure 4.8 shows two dimensional mass-weighted phase diagrams of the gas velocity in the y-axis, and the number of density in the $x-$axis. The image shows the evolution of the phase diagram along the same periods of time as in Figs. 4.1 and 4.2. At $t = 0$, models M2 and M3 indicate the presence of a denser and more massive gas than the distribution of the M1 model. For $\sigma_t = 0\,\mathrm{km\,s^{-1}}$, the majority of gas has a number density $n \sim 1\,\mathrm{cm^{-3}}$, owing to the initial fractal structure of the prescribed density fields in those models. By 0.997 and 1.96 Myr, the model does reflect a major change, however, an increase in the amount of low density gas can be observed in the remaining two models. Then, the gas in the M3 model shows an increment in the concentration of lower-density gas compared with the other two models at times 2.93 and 3.91 Myr. Finally, at 4.89 Myr the number density in the total system has decreased, for example in M3 model the minimum in number density is on the order of $\sim 10^{-8}\,\mathrm{cm^{-3}}$, while for the other two models the minimum is on the order of $\sim 10^{-3}\,\mathrm{cm^{-3}}$, it is possible to note this by the movement of the upper histogram to the left during the whole time period.

In terms of velocity, it is possible to see in Fig. 4.8 how the gas starts with values between 0 to $200\,\mathrm{km\,s^{-1}}$, and as time passes some part of the gas started to increase its velocity. For example, in the model of $\sigma_t = 0\,\mathrm{km\,s^{-1}}$ a certain part of the lower-density (i.e. $n \sim 0.1\,\mathrm{cm^{-3}}$) gas begins to acquire velocity, but in a relatively small way, until it reaches a maximum peak velocity of about $300\,\mathrm{km\,s^{-1}}$ at 2.93 Myr. In the second model of $\sigma_t = 60\,\mathrm{km\,s^{-1}}$, some range of the gas, ($n \sim 1$ to $10\,\mathrm{cm^{-3}}$), reaches velocities slightly above $300\,\mathrm{km\,s^{-1}}$. In the M3 model, there is a considerable increase in velocity compared to the other models, in this case the denser gas has an increase in velocity surpassing $400\,\mathrm{km\,s^{-1}}$ at its highest peak (1.96 Myr), then, some part of the lower-density gas started to gain kinetic

energy.

The change in the number density is caused by the redistribution of the gas, this happens due to two important factors: rotation and thrust of the gas by means of the pressure gradients generated in the central zone, which then trigger interactions with the halo density. Furthermore, the lower-density gas could be related with the expansion of the superbubbles, also, it is possible to find high-density gas which is related with the activity in the Galactic Center and also with the falling of the gas and concentration of it in the central region via gravitational potential.

In addition, the increase in velocity of the lower-density gas is related with the supernova explosions because by the pressure and energy released the gas moves laterally or vertically (in the case of superbubbles), with large velocities in order to overcome the gravitational attraction. Moreover, the presence of less dense gas is associated with the emerge of outflows, starting at 1.96 Myr (see Fig. 4.1), with velocities between 0 and 200 $\mathrm{km\,s^{-1}}$. These factors give us a proof of the formation of winds by the motion of the bubbles surrounded by dense gas, which later, by their merge, will give rise to superbubbles.

4.5   Thermodynamics of superbubbles

The study of thermodynamics in our disc-wind models is also important because it is possible to analyze and understand in a better way certain processes that the gas may undergo, such as heating, winds, shock waves, among others. These phenomena are important to understand the formation of superbubbles. Fig. 4.9 shows the evolution of the gas in a two dimensional temperature-weighted phase diagrams, with the same distribution along both axes as Fig. 4.8.

In Fig. 4.9 it is possible to see for the M1 model high-temperature gas with temperatures above 10^4 K throughout the whole simulation time. The evolution shows that gas heating starts from $t = 0.997$ Myr onwards. This model does not present a loss of gas temperature. For the M2 and M3 models, the initial temperature distribution of the gas ranges from 10 K up to $\sim 10^5$ K, where the high-density gas has lower temperatures. During the evolution of these two models we can observe the appearance of dense gas with high temperatures of 10^7 K reaching velocities greater of $300\,\mathrm{km\,s^{-1}}$ for M2 and $400\,\mathrm{km\,s^{-1}}$ for M3. For the M2 model this appearance is smaller for 0.977 Myr, than in the M3 model, although there is very little gas with high temperature at the same time, and it is much more noticeable for 1.96 Myr. In both models low-density gas emerges with temperatures around $1 - 1000$ K for 0.977 Myr. Nevertheless, the low-density gas starts to heat up as time goes by, in both models whenever low density gas with low temperature appears, it heats up as time passes.

In general, the high-temperature gas reflects the supernova explosions in the Galactic Center via injection of mass and thermal pressure, thus leading to an increase in temperature. Furthermore, the presence of gas with temperature greater than 10^6 K are related with the emission of X-rays, and as consequence a proof of the activity in the central region because of SF processes. In addition, something interesting is that the low-density gas that appears in Fig. 4.9 has low temperatures, which are related with the expansion of the gas, however, this gas start to heat up. One reason for this less dense gas, which is vertically outside the central region, to heat up may be caused by the presence of a wind that generates a shock wave which heats up the gas as it advances. This can explain how the less dense gas shown in Fig. 4.9 increases its temperature. Finally, by the distribution of densities and temperatures, it is

possible to visualise a multiphase structure of the gas, even though the models are adiabatic, which means there is an interchange in the internal energy of the system reflected in the temperature variation. Models with radiative cooling would be desirable to compare against our adiabatic runs.

4.6 Discussion

4.6.1 Comparison to previous work

The exploration of superbubble formation and evolution within our Galaxy has become an increasingly significant topic because it is important for our understanding of the Milky Way's evolution. For this reason it is crucial to mention how the results in our investigation are compared with studies of formation of superbubbles, whether in our own galaxy or in other galaxies.

First, Ponti et al. 2019[9] mentioned the observation of two lobe-like structures in the Galactic Center, which are formed via the continuous injection of energy of feedback events in that region. In this investigation the SN explosions in the active central region of our Galaxy were considered via injection of thermal pressure along time, in a continuous way as proposed by Ponti. Furthermore, according to Ponti et al. 2021[4], the chimneys reach heights of 200 pc, based on recent observations, for our model at 4.89 Myr the superbubbles reach heights above 200 pc, but the height of these structures is changing as time goes by, due to the gravitational attraction of the Galactic Center, a factor that is also mentioned by Ponti et al. 2019[9].

In our investigation the formation of the outflows, which give rise to the superbubbles, start at $t = 0.977$ Myr. On the other hand Cooper et al. 2008[24] states that the merge and formation of the bubbles in their simulation leave the disc by 0.15 Myr. Here, it is important to mention that the simulation of Cooper was based on the data of M82, which is a starburst galaxy. Therefore, the injection of mass and energy is much larger in this galaxy than in the Milky Way, for comparison, the SF rate in our Galaxy is $\sim 0.1 - 1 \, M_\odot \, \text{yr}^{-1}$ and in M82 is $\sim 1 \, M_\odot \, \text{yr}^{-1}$. Furthermore, those outflows are composed of gas with different densities and temperatures, i.e. the gas is multiphase as noted in Nguyen et al. 2022[39]. In the previous section we determined that the flows and gas of the three models are multiphase. Nguyen et al. 2022[39] argues that the hot gas could be observed by X-rays, as mentioned in their paper referring to the hot gas produced by SN explosions.

According to Strickland & Stevens 2000[37], the predominant component of the total energy is the kinetic energy of the hot gas. In Fig. 4.5, it is possible to corroborate the affirmation of Strickland & Stevens, since we have that the kinetic energy has a larger contribution to the total energy of the system. This happens because of the rotation of the gas and for the explosions in the central zone that liberate energy moving the gas hundreds of parsecs in direction of the z-axis, and as Strickland & Stevens this gas is predominantly hot. Indeed, the same authors mention that the winds produced are hot with temperatures of 10^7 K, which coincides with the one found in this research (see Section 4.5).

Furthermore, it is important to mention that the densities inside the bubbles decrease as the distance along the z-axis increases, so they are coherent with the densities observed inside the GC chimneys as Ponti et al. 2019[9] mentioned. Thus, supported by these prior studies we can see that this research provides results that are closely

Figure 4.8: Two dimensional mass-weighted phase diagrams distributions of the velocity and the number of density for three models, over a 4.89-million-year period. The models are located from left to right in the following order $\sigma_t = 0, 60, 100 \text{ km s}^{-1}$, and the evolution goes from the top towards the bottom.
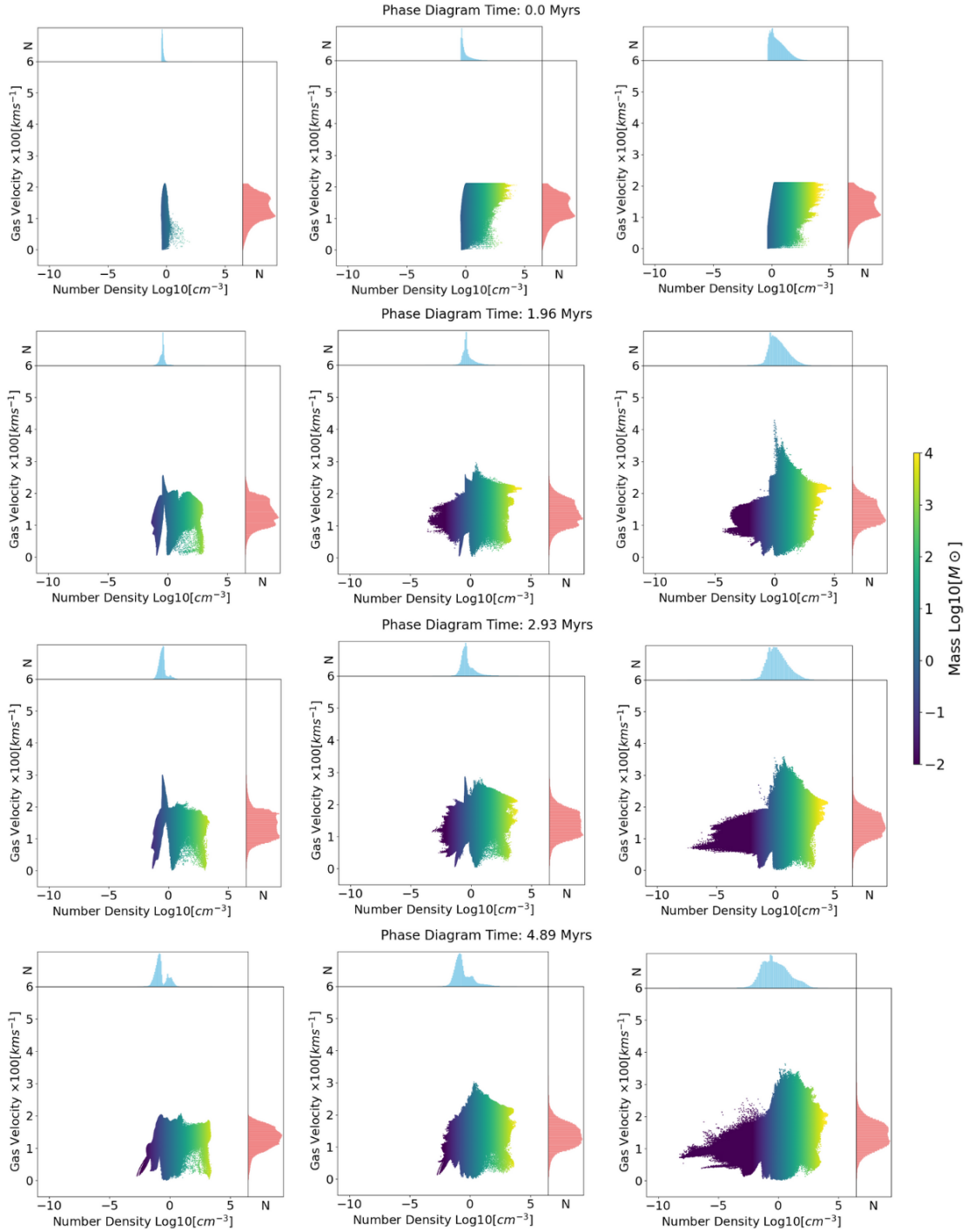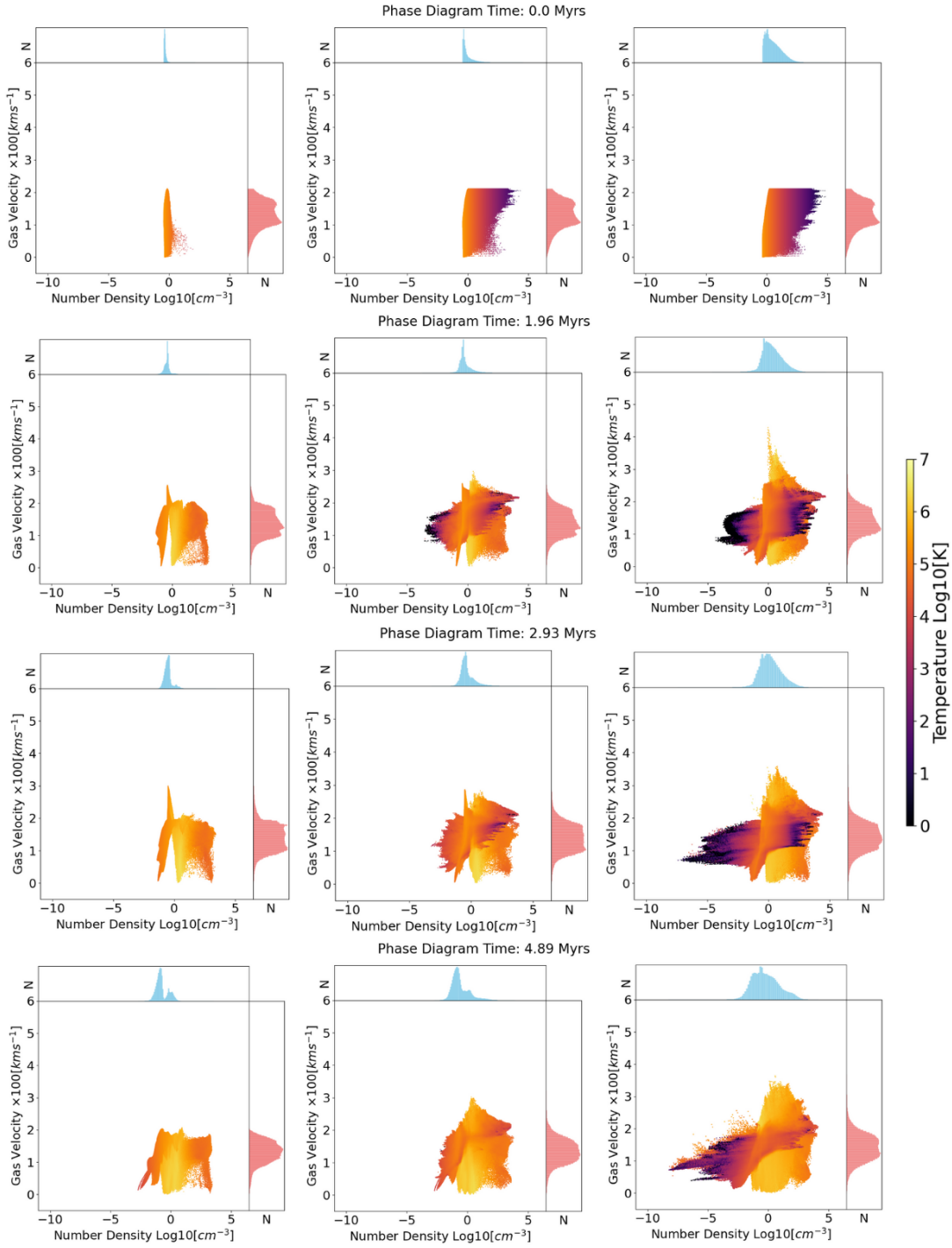
Figure 4.9: Two dimensional temperature-weighted phase diagrams distributions of the velocity and the number of density for three models, over a 4.89-million-year period. The models are located from left to right in the following order $\sigma_t = 0, 60, 100$ km s^{-1}, and the evolution goes from the top towards the bottom.

related to the observations and simulations by other authors. However, the work requires the implementation of additional factors detailed in the following subsection.

4.6.2 Caveats and Limitations

It is important to recognize that this investigation does not consider some factors, which may be dynamically important for the global modelling of the nuclear wind of our Galaxy, so it has limitations, which can be systematically addressed in future studies. The Milky Way is a complex system and it has many physical processes, most of them are already considered in this project, but some others are missing. Those factors are crucial and should eventually be implemented in the simulation because they could have an effect in the formation and evolution of the superbubbles.

Once the SN feedback ejects mass out of the disc, the direction in which the gas expands in this project is only influenced by the gas density and gravitational potential. In addition to the injection conditions. However, the shock wave produced as bubbles expand could ionize some of the gas on the wavefront, and could do so differently for distinct orientations of the magnetic field. Thus some physical process that could be crucial and are not considered yet are possible gas metallicity changes and the magnetic field of our Galaxy. Therefore, studying models with spatially-dependent metallicities and magnetohydrodynamic (MHD) scenarios are important to implement because they could have an impact in the dynamics of the gas specially for dense gas (see Banda-Barragan et al. 2018[48]). Moreover, they could affect the distribution of the gas and as consequence the injection of mass and energy, which could change in some way the evolution of the superbubbles, e.g. outflows have been shown to be channeled out of starburst galaxies by a poloidal magnetic field component (see. Lopez-Rodriguez et al. 2021[49]).

Another process to be implemented would be radiative cooling, as we know the system we are studying is not completely adiabatic, but loses internal energy in the form of radiation as Smith et al. 2017[50] mentioned. Our galaxy, and specifically the superbubbles under investigation, is forged within a region characterized by intense SF. On average, this region exhibits low densities. According to Draine 2010[51], the collisional excitation of ions, in regions with low-densities, result in a radiative cooling.

Radiative cooling plays a significant role in the formation of many astrophysical objects, and it is important to determine the line of evolution of the object that will be formed (see Smith et al. 2017[50]; Wiersma et al. 2009[52]; Turk et al. 2011[53]). The process leads with the reciprocal action between the dust and the gas, which in fact is a very complex chemical interaction. In a general view, the radiative cooling depends on the following factors; chemical composition, temperature, ionization balance, density of the gas, and radiation field.

There are types of radiative cooling, that depend on the temperature, for example, recombination is a process by which ionized hydrogen atoms try to return to the ground state, but for this they need to eject some energy, the photons that are emitted are one form to cooling the gas, this process dominates the low-temperature gas ($T < 10^5 K$). Another way, that is much more efficient than recombination, is the line emission of ions of heavier atoms (see Maoz 2016[8]), here the protons collide with some ions of the heavier atoms and excite them, (i.e. takes some kinetic energy), therefore reaching a collisional excitation, if there is not a deexcitation of the ion that returns the energy that it takes, then this ion could decay and the resulting photons carries away the energy, cooling the gas. A third way to cool the gas is the bremsstrahlung (free–free) emission, which is about the deceleration of a free electron by

interaction with electromagnetic fields of the gas ions, thus emitting radiation, and therefore, cooling the gas. The latter process is dominant in high-temperature gas ($T > 10^7$ K) (see Villares 2023[54]).

However, at very large resolutions, such as those of this research or higher, the application of this phenomenon to the gas can lead to numerical errors, so we must be careful with the implementation of this process.

In addition, another type of boundary condition could be implemented in order to avoid the loss of mass from the system, on the other hand, the analysis could focus in the central region, for example our model consider the range of (-700 , 700) pc, so the analysis could be made in a smaller region of (-400 , 400) pc. That way, the influence of the loss of mass on the results would be minimised. Furthermore, the analysis of the models could be extended, for example a two dimensional velocity map of the simulation or a two dimensional temperature map. Such maps can help us to better observe the formation of the superbubbles, especially the temperature map. In brief, it is important to take into account all the needed implementations for future simulations, particularly radiative cooling.

4.6.3   Resolution Effects

The numerical resolution of the simulations can affect the results to a certain extent. With the aim of analyzing the impact of numerical resolution on our analysis, two additional models were carried out for the M2 model with $\sigma_t = 60$ km s^{-1} value, with half its resolution and a quarter of its resolution, i.e.,($160 \times 160 \times 160$) and ($80 \times 80 \times 80$), respectively. In Figs. 4.10 and 4.11 it is possible to observe the time evolution of the model for different numerical resolutions. The two figures show two different slices of the models, one with a side view and one with a top view.

The first observation that can be made is that although the resolution is different, the plots at time 0 Myr indicate the same gas distribution. However, as time passes the differences caused by the resolution are evident in gas evolution. For the lower resolution case, the outflows appear to reach higher heights due to the presence of a larger amount of dense gas in the SF region. On the other hand, in the half-resolution model the concentration of much more dense gas is still noticeable compared to the high-resolution model, but the bubbles, unlike the structure, reach approximately the same height as those observed in the high-resolution model. Besides, there is also the presence of filaments in the disc part, which is not seen in the low-resolution model (see Fig. 4.10).

In addition, from the top view all the simulations present the formation of a rotating disc, nevertheless, in the case of the low-resolution model the gas distribution seems to be more homogeneous. In other words, there is not much presence of regions where dense gas is found close to low-density gas as in the high-resolution model, moreover, the central zone does not show high-density gas as the higher resolution M2 model. In the gas of the medium-resolution model it is already possible to observe the regions with different densities, but this difference is not as big as in the high-resolution model, and the central zone does not indicate the presence of so much dense gas as in the higher resolution M2 model (see Fig. 4.11).

Regarding the analysis of density, pressure, internal energy and total mass, the numerical resolution has an effect in the magnitudes of all those quantities. Figure 4.12 shows the numerical analysis of the three resolution models as a function of time. First, in the average density plot we can see that the high and half-resolution models converge in the magnitude of the density, whereas, the low-resolution simulation shows a decrease in the magnitude of the average density of the system. Therefore, the low-resolution run underestimates the density. In addition, the

Figure 4.10: Time evolution for a cross section in the x=0 axis. Resolution decreases from left to right with high $(320 \times 320 \times 320)$, medium $(160 \times 160 \times 160)$ and low $(80 \times 80 \times 80)$ resolution respectively.

.
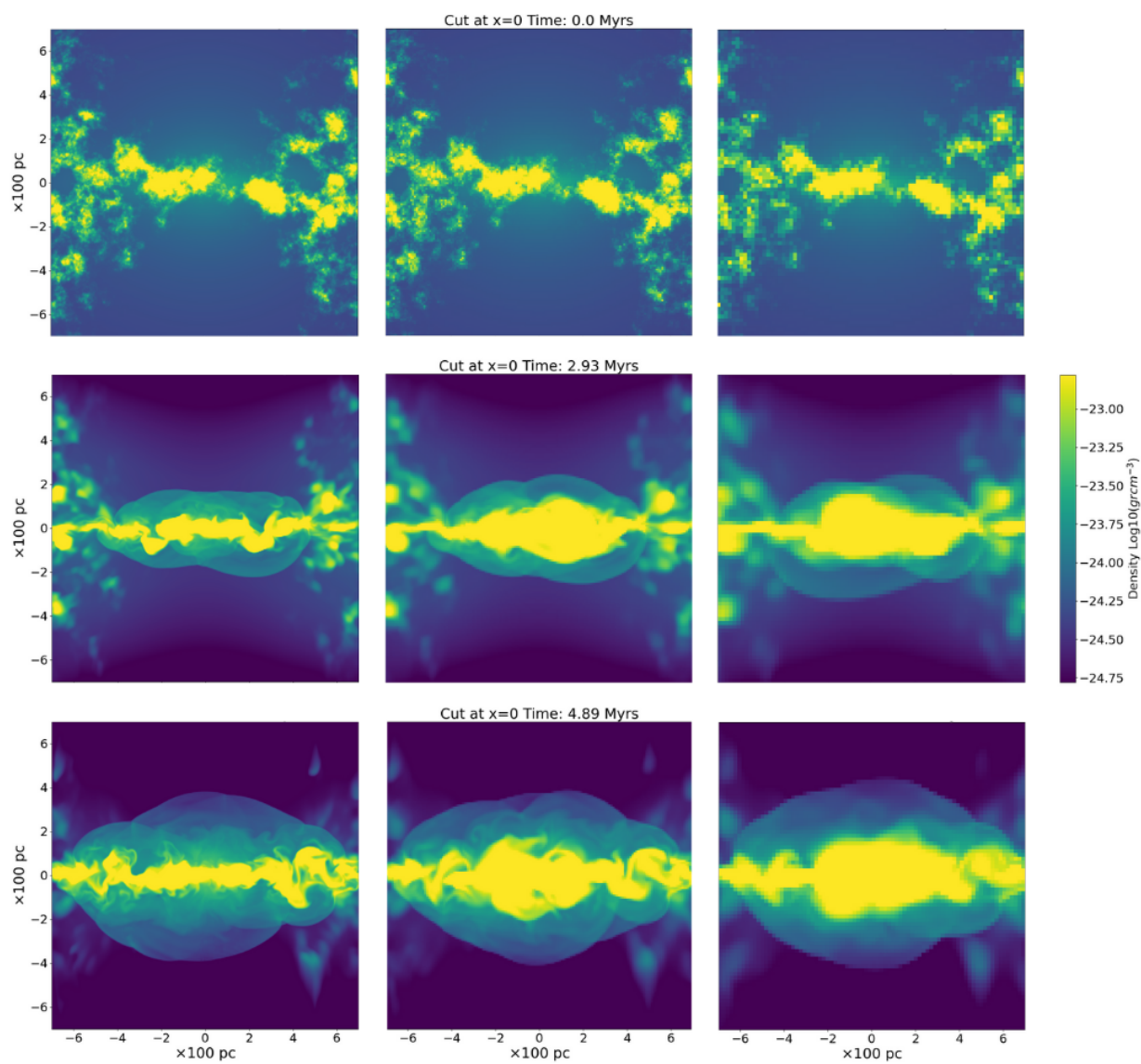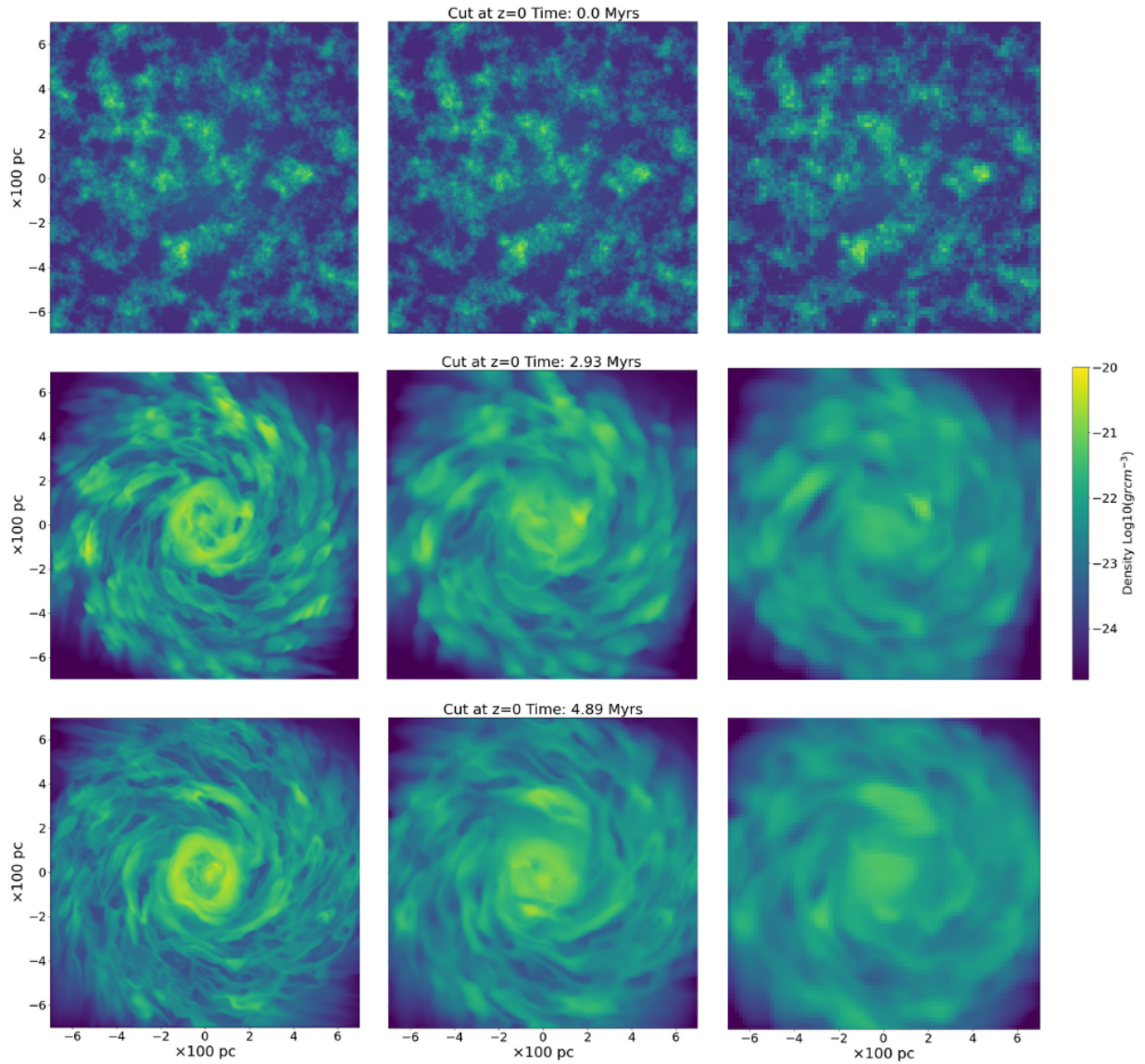
Figure 4.11: Time evolution for a cross section in the z=0 axis. Resolution decreases from left to right with high $(320 \times 320 \times 320)$, medium $(160 \times 160 \times 160)$ and low $(80 \times 80 \times 80)$ resolution respectively.

.

standard deviation of gas density increases as the resolution increases, the reason for this change was explained in the analysis of the gas distribution as seen from the top for Fig. 4.11. This quantity increases as time passes only for the high-resolution model, because of the density differences in the central region and inside the bubbles, which are better captured at. higher resolutions.

Furthermore, the plot of average gas pressure shows a similar path followed by the increase in pressure for the three resolution models. However, the magnitude of pressure in each simulation is not the same, the pressure in models with less resolution is higher due to the concentration of dense gas in the central region and a thick disc forms by the decrease in resolution. Thus the injection of pressure is greater in models with lower numerical resolution. Additionally, the standard deviation seems to converge for the half and low resolution models, although the path of the curves is not the same, the separation between convergence in the standard deviation of the pressure of the higher resolution models. However, the space is a little larger due to certain periodicity of the curve, and also in the final times of the simulation.

The last row of Fig. 4.12 shows the internal energy and the total mass of the gas, both of which are measures derived from the density and pressure. They also undergo a change in magnitude, as the resolution decreases so does the order of magnitude of these quantities as more dense gas from the initial fractal distribution is captured with higher resolutions. Something interesting to note is that the curves of the three models follow the same trend, i.e. they have the same shape of the curve, which indicates that the internal processes are the same only in smaller or larger quantities depending on the resolution as this is influenced by the distribution of the gas.

In sum, even when the started points in density, pressure and their standard deviation plots is the same, the curves do not show convergence in absolute values, with the exception of the medium and high resolution models only for the density plot, and to a lesser extent for the standard deviation of pressure. Despite this, we notice that the curves do have very similar trends when scaled. Furthermore, due to the change in the mentioned magnitudes the quantities derived from them, which are the internal energy and total mass, also change in remarkable orders of magnitude. Finally, the shape of the curve, for the average of density and pressure and also for the internal energy and total mass, is similar in form. This indicates that despite the difference in resolution and the over or under estimation of certain quantities, the internal processes occurring in the simulations are the same, reflecting these trends in the quantities under analysis. Moreover, although the variation in the numerical resolution, it is still possible to see the formation of superbubbles.
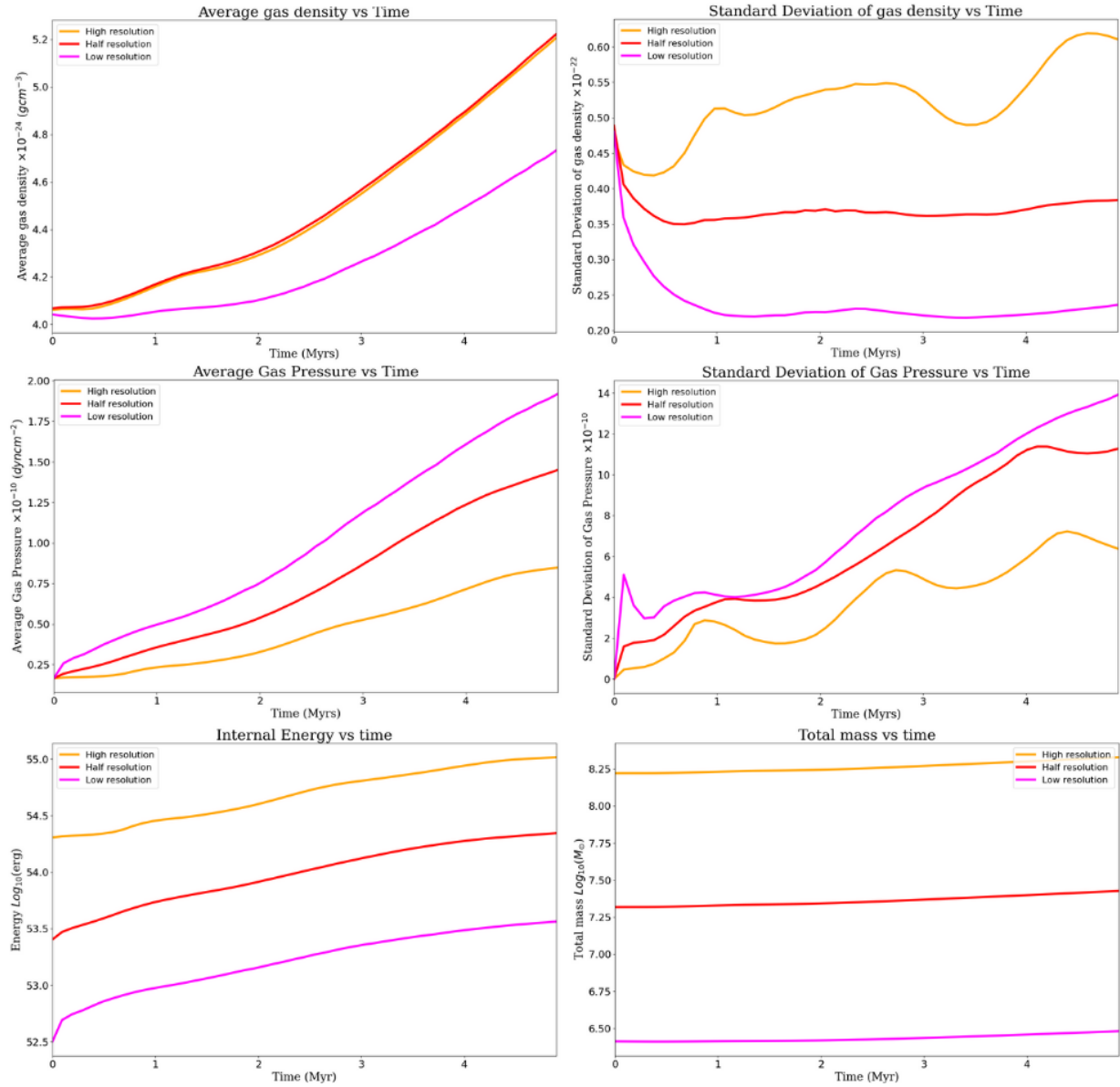
Figure 4.12: Converge analysis for density, pressure, internal energy and total mass of three resolution models as a function of time.

Chapter 5

Conclusions & Outlook

The Milky Way is a complex system hosting a variety of feedback processes. In the Galactic centre, for example, two lobe-like structures have been observed (one extending to the north and one to the south), which point to the presence of galactic outflows. Such outflows are important because they act as a feedback mechanism between the ISM and the CGM. In order to analyze in a deeper way the formation and evolution of galactic superbubbles, computational simulations are required. In this thesis, we have implemented a gravitational potential with the data of our Galaxy. With such potential, we have studied 3 models with different values of the turbulence parameter (σ_t), which generated different initial gas distributions in the primordial atmosphere of the Galaxy. This was implemented with self-consistent rotational velocities and density distributions, as they are dependent on the gravitational potential. Furthermore, we applied diode boundary conditions in order to avoid the re-entry of gas into the computational domain. In addition, the activity in the Galactic Center was simulated by the injection of mass and energy as thermal pressure, with which we replicated the action of an intense SF zone. The purpose of this research was to evaluate the formation and evolution of superbubbles due to different initial conditions ($\sigma_t = 0, 60, 100 \text{ km s}^{-1}$), for which the main findings are detailed below:

- The global evolution of the superbubbles can be described by the following steps: first, it is necessary an initial distribution of the gas, then the gas is redistributed by the action of the gravitational potential and also by the rotation velocity. After that, the injection process occurs via several SN explosions, which eject mass and energy, thus increasing the density in the central region. Then, by the action of thermal pressure, several outflows are formed, ejecting the material in all directions. Such outflows propagate more to the sides in models M1, M2 than in model M3 (where lateral expansion is limited by the thicker disc). Finally, the gas expands mostly vertically leading to the formation of superbubbles that reach heights of hundreds of parsecs depending on the initial distribution of the gas (see Section 4.1).

- The simulations have also demonstrated the formation of a rotating disc for two of the models (M2 and M3) due to the rotation that was implemented based on the gravitational potential, thus giving an idea of how the density distribution in the medium has an impact on the creation of the inner ISM disc in our Galaxy.

Furthermore, the implementation of the rotational velocity is important as it allows to counterbalance the effect of the gravitational potential, otherwise all the gas would collapse very quickly into the center (see Section 4.1).

- The turbulence parameter (σ_t), in addition to controlling the disc scale height, also has an impact on different quantities such as density, mass, pressure, and energy. It controls, via gas re-distribution, the rate at which these variables change over time. As the σ_t value increases, the density and as consequence the mass also increase. Moreover, with more material in the SF zone the increment in the activity of supernovae produces an increase in pressure, which leads to pressure gradients and the emergence of winds. Furthermore, the energy increases as the value of this parameter increases. For modest values of σ_t the increase in internal energy seems to have periodicity, but for larger values, as in the M3 model, the energy increases very fast and the gas becomes dissipative. Finally, the increment in this turbulence parameter produces an increase in the magnitudes of our analysis as density, pressure, total and internal energy, and total mass. Nevertheless, the standard deviation of the density and pressure distribution in the whole computational domain is lower because the distribution is more uniform for $\sigma_t = 0, 60\,\mathrm{km\,s^{-1}}$ (see Section 4.2).

- The study of kinematics has shown the presence of outflows that can originate bubbles, which through their merge will form superbubbles. The variation in the gas number density and the increase in velocity for lower and higher density gas are the evidence of the expansion of the bubbles that cause the formation of winds in the medium, and as consequence, the superbubble formation. Furthermore, the high velocities in the medium are in relation with the formation of winds, which play a significant role in the formation of superbubbles. Moreover, it is important to mention that thicker discs, i.e. $\sigma_t > 60\,\mathrm{km\,s^{-1}}$, lead to more realistic scenarios, regarding comparisons to the GC wind (see Section 4.4).

- In the thermodynamic analysis of the simulation, it was possible to observe the production of hot gas resulting from SNe in the central region reaching high temperatures. In addition, the presence of a shock wave due to the formation of winds by the expansion of the gas at high velocities, thus heating more diffuse gas in the halo. In short, this analysis indicates a multiphase gas that is changing due to the expansion of the bubbles from the center (see Section 4.5).

- The adiabatic models present a distribution in densities over time. There is the presence of dense gas with low density. In addition, we also see a changing temperature resulting from the exchange of internal energy in the system. It is interesting to mention that the gas is not only heated because it is an adiabatic simulation, but also that we observe adiabatic cooling in two models (M2 and M3). These factors give rise to a multiphase gas, whose mixing is the result of the explosions of the central region and the formation of shock waves that are at the front of the expanding bubble (see Section 4.5).

In summary, this thesis provides important insights into the study of superbubbles as we reveal that the initial density structure of the ISM disc can lead to distinct scenarios, with thicker discs favouring the formation of outflows. In addition, this project helps significantly to understand the process of formation of superbubbles. From

the observations made is very difficult to get clear ideas of what could have happened as we are looking at a single snapshot in time. In our simulations, on the other hand, we can follow the formation of superbubbles from t=0 and for several Myr. It is also difficult to obtain 3D information from observational data as they show only a projection, while in our simulations we can make three-dimensional plots and carry out different projections, allowing a better understanding of the formation and evolution of superbubbles.

We recommend that future work considers the implementation of new physical processes, particularly the influence of magnetohydrodynamics (MHD) and radiative cooling, with the aim of making simulations more realistic. In addition, a goal for future work is to explain why the two superbubbles in our Galaxy have a difference in shape, namely the northern superbubble is more spherical while the southern superbubble is more elongated, if they share the same origin and composition.

Bibliography

[1] Mann, A. "Fermi" bubbles are bursting from our galaxy. Their origins remain a mystery. *Proceedings of the National Academy of Science* **2023**, *120*, e2318720120.

[2] Sofue, Y. Is M82 a Disk-Truncated Bulge by a Close Encouter with M81? *Publications of the Astronomical Society of Japan* **1998**, *50*, 227–231.

[3] Xiang, M.; Rix, H.-W. A time-resolved picture of our Milky Way's early formation history. **2022**, *603*, 599–603.

[4] Ponti, G.; Morris, M.; Churazov, E.; Heywood, I.; Fender, R. The Galactic center chimneys: the base of the multiphase outflow of the Milky Way. *Astronomy & Astrophysics* **2021**, *646*, A66.

[5] Tumlinson, J.; Peeples, M. S.; Werk, J. K. The circumgalactic medium. *Annual Review of Astronomy and Astrophysics* **2017**, *55*, 389–432.

[6] Mayya, Y.; Alzate, J.; Lomelí-Núez, L.; Zaragoza-Cardiel, J.; Gómez-González, V.; Silich, S.; Fernández-Arenas, D.; Vega, O.; Ovando, P.; Rodríguez, L. The stellar population responsible for a kiloparsec-size superbubble seen in the JWST 'phantom'images of NGC 628. *Monthly Notices of the Royal Astronomical Society* **2023**, *521*, 5492–5507.

[7] Carraro, G. *Astrophysics of the interstellar medium*; Springer, 2021.

[8] Maoz, D. *Astrophysics in a Nutshell*; Princeton university press, 2016; Vol. 16; p 64.

[9] Ponti, G.; Hofmann, F.; Churazov, E.; Morris, M.; Haberl, F.; Nandra, K.; Terrier, R.; Clavel, M.; Goldwurm, A. An X-ray chimney extending hundreds of parsecs above and below the Galactic Centre. *Nature* **2019**, *567*, 347–350.

[10] Veena, V. S.; Riquelme, D.; Kim, W. J.; Menten, K. M.; Schilke, P.; Sormani, M. C.; Banda-Barragán, W. E.; Wyrowski, F.; Fuller, G. A.; Cheema, A. A CO funnel in the Galactic centre: Molecular counterpart of the northern Galactic chimney. **2023**, *674*, L15.

[11] Cicone, C.; Maiolino, R.; Marconi, A. Outflows and complex stellar kinematics in SDSS star-forming galaxies. **2016**, *588*, A41.

[12] Dawson, J. R. The Supershell - Molecular Cloud Connection: Large-Scale Stellar Feedback and the Formation of the Molecular ISM. **2013**, *30*, e025.

[13] Snowden, S. L.; Egger, R.; Finkbeiner, D. P.; Freyberg, M. J.; Plucinsky, P. P. Progress on Establishing the Spatial Distribution of Material Responsible for the 1 4 keV Soft X-Ray Diffuse Background Local and Halo Components. **1998**, *493*, 715–729.

[14] Crocker, R. M. Non-thermal insights on mass and energy flows through the Galactic Centre and into the Fermi bubbles. **2012**, *423*, 3512–3539.

[15] Nakashima, S.; Koyama, K.; Wang, Q. D.; Enokiya, R. X-ray observation of a magnetized hot gas outflow in the galactic center region. *The Astrophysical Journal* **2019**, *875*, 32.

[16] Predehl, P.; Sunyaev, R.; Becker, W.; Brunner, H.; Burenin, R.; Bykov, A.; Cherepashchuk, A.; Chugai, N.; Churazov, E.; Doroshenko, V. Detection of large-scale X-ray bubbles in the Milky Way halo. *Nature* **2020**, *588*, 227–231.

[17] Heywood, I.; Camilo, F.; Cotton, W.; Yusef-Zadeh, F.; Abbott, T.; Adam, R.; Aldera, M.; Bauermeister, E.; Booth, R.; Botha, A. Inflation of 430-parsec bipolar radio bubbles in the Galactic Centre by an energetic event. *Nature* **2019**, *573*, 235–237.

[18] Zhang, M.; Li, Z.; Morris, M. R. A supernova-driven, magnetically collimated outflow as the origin of the galactic center radio bubbles. *The Astrophysical Journal* **2021**, *913*, 68.

[19] McClure-Griffiths, N. M.; Ford, A.; Pisano, D. J.; Gibson, B. K.; Staveley-Smith, L.; Calabretta, M. R.; Dedes, L.; Kalberla, P. Evidence for Chimney Breakout in the Galactic Supershell GSH 242–03+ 37. *The Astrophysical Journal* **2006**, *638*.

[20] Zhou, X.; Su, Y.; Yang, J.; Chen, X.; Sun, Y.; Jiang, Z.; Wang, M.; Wang, H.; Zhang, S.; Xu, Y. A Systematic Study of Associations between Supernova Remnants and Molecular Clouds. *arXiv preprint arXiv:2308.03484* **2023**,

[21] Sánchez-Cruces, M.; Rosado, M. Hα kinematics of superbubbles and supernova remnants of the dwarf galaxy NGC 4214. *Monthly Notices of the Royal Astronomical Society* **2023**, *524*, 4907–4922.

[22] Carretti, E.; Crocker, R. M.; Staveley-Smith, L.; Haverkorn, M.; Purcell, C.; Gaensler, B. M.; Bernardi, G.; Kesteven, M. J.; Poppi, S. Giant magnetized outflows from the centre of the Milky Way. **2013**, *493*, 66–69.

[23] Su, M.; Slatyer, T. R.; Finkbeiner, D. P. Giant Gamma-ray Bubbles from Fermi-LAT: Active Galactic Nucleus Activity or Bipolar Galactic Wind? **2010**, *724*, 1044–1082.

[24] Cooper, J. L.; Bicknell, G. V.; Sutherland, R. S.; Bland-Hawthorn, J. Three-dimensional simulations of a starburst-driven galactic wind. *The Astrophysical Journal* **2008**, *674*, 157.

[25] Schneider, E. E.; Robertson, B. E. Hydrodynamical coupling of mass and momentum in multiphase galactic winds. *The Astrophysical Journal* **2017**, *834*, 144.

[26] Banda-Barragán, W. E.; Brüggen, M.; Heesen, V.; Scannapieco, E.; Cottle, J.; Federrath, C.; Wagner, A. Y. Shock-multicloud interactions in galactic outflows - II. Radiative fractal clouds and cold gas thermodynamics. **2021**, *506*, 5658–5680.

[27] Schneider, E. E.; Ostriker, E. C.; Robertson, B. E.; Thompson, T. A. The Physical Nature of Starburst-driven Galactic Outflows. **2020**, *895*, 43.

[28] Oppenheimer, B. D.; Davé, R. Mass, metal, and energy feedback in cosmological simulations. *Monthly Notices of the Royal Astronomical Society* **2008**, *387*, 577–600.

[29] Gribbin, J. *Galaxies: A very short introduction*; Oxford University Press, USA, 2008; Vol. 182.

[30] Robertson, B. E. Galaxy formation and reionization: key unknowns and expected breakthroughs by the james webb space telescope. *Annual Review of Astronomy and Astrophysics* **2022**, *60*, 121–158.

[31] Hernández-Aguayo, C.; Arnold, C.; Li, B.; Baugh, C. M. Galaxy formation in the brane world I: overview and first results. *Monthly Notices of the Royal Astronomical Society* **2021**, *503*, 3867–3885.

[32] Majewski, S. Galactic structure surveys and the evolution of the Milky Way. *Annual review of astronomy and astrophysics* **1993**, *31*, 575–638.

[33] Shuter, W. L. H. *Kinematics, Dynamics and Structure of the Milky Way: Proceedings of a Workshop on "The Milky Way" Held in Vancouver, Canada, May 17–19, 1982*; Springer Science & Business Media, 2012; Vol. 100.

[34] Morris, M.; Serabyn, E. The galactic center environment. *Annual Review of Astronomy and Astrophysics* **1996**, *34*, 645–701.

[35] Armijos-Abendaño, J.; Banda-Barragán, W.; Martín-Pintado, J.; Dénes, H.; Federrath, C.; Requena-Torres, M. A. Structure and kinematics of shocked gas in Sgr B2: further evidence of a cloud–cloud collision from SiO emission maps. *Monthly Notices of the Royal Astronomical Society* **2020**, *499*, 4918–4939.

[36] Nogueras-Lara, F. Hunting young stars in the Galactic centre. Hundreds of thousands of solar masses of young stars in the Sagittarius C region. **2024**, *681*, L21.

[37] Strickland, D. K.; Stevens, I. R. Starburst-driven galactic winds—I. Energetics and intrinsic X-ray emission. *Monthly Notices of the Royal Astronomical Society* **2000**, *314*, 511–545.

[38] Heckman, T. M.; Thompson, T. A. Galactic winds and the role played by massive stars. *arXiv preprint arXiv:1701.09062* **2017**,

[39] Nguyen, D. D.; Thompson, T. A.; Schneider, E. E.; Lopez, S.; Lopez, L. A. Dynamics of hot galactic winds launched from spherically-stratified starburst cores. *arXiv arXiv:2210.07193v2 [astro-ph.GA]* **2022**,

[40] Della Ceca, R.; Griffiths, R. E.; Heckman, T. M. Starburst-driven Outflows in Low-Luminosity Galaxies: ASCA and ROSAT Observations of NGC 4449. *The Astrophysical Journal* **1997**, *485*, 581.

[41] Heckman, T. M.; Armus, L.; Miley, G. K. On the nature and implications of starburst-driven galactic superwinds. *Astrophysical Journal Supplement Series (ISSN 0067-0049), vol. 74, Dec. 1990, p. 833-868. Research supported by NSF and NASA.* **1990**, *74*, 833–868.

[42] Beirão, P.; Armus, L.; Lehnert, M.; Guillard, P.; Heckman, T.; Draine, B.; Hollenbach, D.; Walter, F.; Sheth, K.; Smith, J.; et al., Spatially resolved Spitzer-IRS spectral maps of the superwind in M82. *Monthly Notices of the Royal Astronomical Society* **2015**, *451*, 2640–2655.

[43] Chevalier, R.; Clegg, A. W. Wind from a starburst galaxy nucleus. *Nature* **1985**, *317*, 44–45.

[44] Banda-Barragán, W. E.; Zertuche, F. J.; Federrath, C.; García Del Valle, J.; Brüggen, M.; Wagner, A. Y. On the dynamics and survival of fractal clouds in galactic winds. **2019**, *486*, 4526–4544.

[45] Mignone, A.; Bodo, G.; Massaglia, S.; Matsakos, T.; Tesileanu, O. e.; Zanni, C.; Ferrari, A. PLUTO: a numerical code for computational astrophysics. *The Astrophysical Journal Supplement Series* **2007**, *170*, 228.

[46] Childs, H. *et al. High Performance Visualization–Enabling Extreme-Scale Scientific Insight*; 2012; pp 357–372.

[47] Toro, E. F. The hllc riemann solver. *Shock Waves* **2019**, *29*, 1065–1082.

[48] Banda-Barragán, W.; Federrath, C.; Crocker, R.; Bicknell, G. Filament formation in wind–cloud interactions–II. Clouds with turbulent density, velocity, and magnetic fields. *Monthly Notices of the Royal Astronomical Society* **2018**, *473*, 3454–3489.

[49] Lopez-Rodriguez, E.; Guerra, J. A.; Asgari-Targhi, M.; Schmelz, J. T. The Strength and Structure of the Magnetic Field in the Galactic Outflow of Messier 82. **2021**, *914*, 24.

[50] Smith, B. D.; Bryan, G. L.; Glover, S. C. O.; Goldbaum, N. J.; Turk, M. J.; Regan, J.; Wise, J. H.; Schive, H.-Y.; Abel, T.; Emerick, A.; O'Shea, B. W.; Anninos, P.; Hummels, C. B.; Khochfar, S. GRACKLE: a chemistry and cooling library for astrophysics. *Monthly Notices of the Royal Astronomical Society* **2017**, *466*, 2217–2234.

[51] Draine, B. T. *Physics of the interstellar and intergalactic medium*; Princeton University Press, 2010; Vol. 19.

[52] Wiersma, R. P.; Schaye, J.; Smith, B. D. The effect of photoionization on the cooling rates of enriched, astrophysical plasmas. *Monthly Notices of the Royal Astronomical Society* **2009**, *393*, 99–107.

[53] Turk, M. J.; Clark, P.; Glover, S. C.; Greif, T. H.; Abel, T.; Klessen, R.; Bromm, V. Effects of varying the three-body molecular hydrogen formation rate in primordial star formation. *The Astrophysical Journal* **2010**, *726*, 55.

[54] Villares, A. Unravelling the multi-scale and turbulent structure of galactic winds. 2023.